sec each at 60% maximum setting of the sonicator (Handy Sonic-UR-20P, TOMY SEIKO Co., Ltd., Tokyo, Japan). Sonicated cell supernatant was diluted 10-fold, and 1% (20 μl) of the total diluted lysate was used for total genomic DNA as input DNA control. The rest (1980 μl) was then subjected to immunoclearing by 75 μl salmon sperm DNA/protein A agarose-50% slurry for 30 min at 4 C. Immunoprecipitation was performed for overnight at 4 C with 3 μg p65 antibody (Santa Cruz Biotechnology). For negative control, normal rabbit IgG (Santa Cruz Biotechnology) was used instead of p65 antibody. Precipitates were washed sequentially for 5 min each in low salt, high salt, LiCH immune complex wash buffers, and finally washed twice with Tris/EDTA buffer. Histone complexes were then eluted from the antibody by freshly prepared elution buffer (1% SDS, 0.1 M $NaHCO_3$). Histone-DNA cross-links (including the input samples) were reversed by 5 M NaCl at 65 C for 4 h. DNA fragments were extracted with a PCR purification kit (Qiagen). One microliter from a 30-μl DNA extraction was used for PCR and primed by sequences as follows: forward, 5′-GGG AAG AAG ATT GCC TAA AC-3′; reverse, 5′-TGT GGA AAT CAA AGG GAC AG-3′; the PCR size was 401 bp.

Real-time PCR

Immunoprecipitated DNA samples were then set to real-time PCR analysis to quantify the relative amount to their corresponding input controls with a LightCycler (Roche Diagnostics GmbH, Mannheim, Germany) according to the manufacturer's instruction. Briefly, 1 μl immunoprecipitated DNA sample (or H_2O as negative control), was placed into a 20-μl reaction volume containing 1 μl of each primer (10 μM) and 2 μl LightCycler-FastStart DNA Master SYBR Green I (Roche), which includes nucleotides, Tag DNA polymerase, and buffer. PCR products were visualized on a 2% agarose gel and finally validated by direct sequencing. Input samples were amplified simultaneously as the internal controls. Real-time PCR data for each immunoprecipitated sample were calculated as a ratio to its corresponding input sample. Briefly, threshold values (crossing line) obtained where fluorescent intensity was in the geometric phase, cycle number at the crossing point of an immunoprecipitated sample (Cip), and the corresponding input sample (Cco) were determined via LightCycler software version 3.5. The relative amount to input sample of the immunoprecipitated sample (Aip) was calculated by the formula of: $Aip = 2^{(Cco-Cip)}$.

Statistics

One-way ANOVA followed by Scheffé's test was used for multigroup comparisons.

Results

TGZ+LG inhibited ArPII dose-dependently

We previously reported that TGZ+LG inhibit aromatase activity, and consistently the estrone production, in a dose-dependent manner (23). We also found that TGZ+LG down-regulated aromatase mRNA by both decreased transcription and increased degradation. Here a 4.0-kb fragment of human ArPII was inserted into PGL3-Basic to make the luciferase reporter PGL3-ArPII and then used to further address whether TGZ, LG, or TGZ+LG interfered with the transcription of aromatase from promoter II. KGN cells were transfected by Superfect with PGL3-ArPII as well as the internal control phRL-CMV. As shown in Fig. 1, on the addition of increasing concentration of TGZ+LG, the relative luciferase activity was decreased in a concentration-dependent manner. Although they were weaker, TGZ or LG alone also manifested inhibitory effects on ArPII. The results indicate that the inhibitory effect of TGZ+LG on aromatase gene is directly mediated by the inhibition of promoter II activity.

PPARγ is critical for the TGZ+LG inhibition

To further clarify the involvement of PPARγ in the regulation of ArPII, the same experiment as described above was carried out in NIH-3T3 cells, which lack endogenous expression of PPARγ (26). As shown in Fig. 2A, neither TGZ (or LG) alone nor combined treatment of TGZ+LG could decrease the expression of the PGL3-ArPII reporter, even when the concentration was raised to 10 μM for TGZ and 1.0 μM for LG, when the cells had been cotransfected with PGL3-ArPII+phRL-CMV and pcDNA3.1, the empty vector. However, on the exogenous cotransfection of the PPARγ expression vector, either TGZ or LG alone significantly decreased ArPII activity in a concentration-dependent manner, and combined treatment of TGZ+LG caused a sharper decrease in expression from the promoter. This phenomenon nicely mimicked what was observed in KGN cells, which possess endogenous PPARγ. These data clearly demonstrate the involvement of PPARγ in the inhibition of ArPII.

NF-κB inhibitors abolished the inhibition of TGZ+LG on aromatase gene

Due to the absence of a PPARγ-RXR-responsive element in the aromatase promoter II (23), we previously suggested that PPARγ might inhibit the promoter by an indirect mechanism (23). This hypothesis is supported by recent work (27), which showed that there was no binding of PPARγ and RXRα heterodimers to the promoter. A series of studies pointed out the inhibitory effect of PPARγ activation on NF-κB-dependent transcription system (28–30). We thus tested the possibility that PPARγ activation inhibits aromatase gene through the NF-κB system by using specific inhibitors for NF-κB: CAPE (31) and APDC (32). CAPE specifically inhibits NF-κB binding to DNA and also prevents the translocation of the p65 subunit of NF-κB to the nucleus and delays IκBα

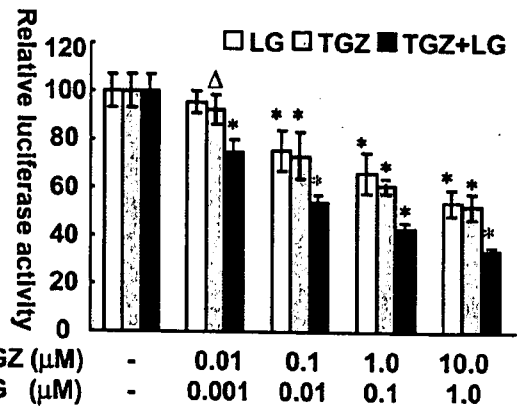

FIG. 1. TGZ+LG inhibits aromatase promoter II. The luciferase reporter PGL3-ArPII, wherein the luc+ gene is driven by a 4.0-kb segment of the human ArPII, was transfected into KGN cells, which were seeded in 12-well plates 1 d earlier. The cells were treated with an increasing concentration (as indicated) of TGZ, LG, or TGZ+LG 1 d after transfection for 24 h. Cells were then lysed and a dual-luciferase reporter assay was performed. The ArPII-mediated firefly luciferase signal was normalized using *Renilla* luciferase, which was constitutively expressed by the internal control phRL-CMV vector. Data expressed in mean ± SD was from identically treated triplicate samples of three independent experiments. Δ, $P < 0.05$; *, $P < 0.01$, compared with basal level of the same treatment group.

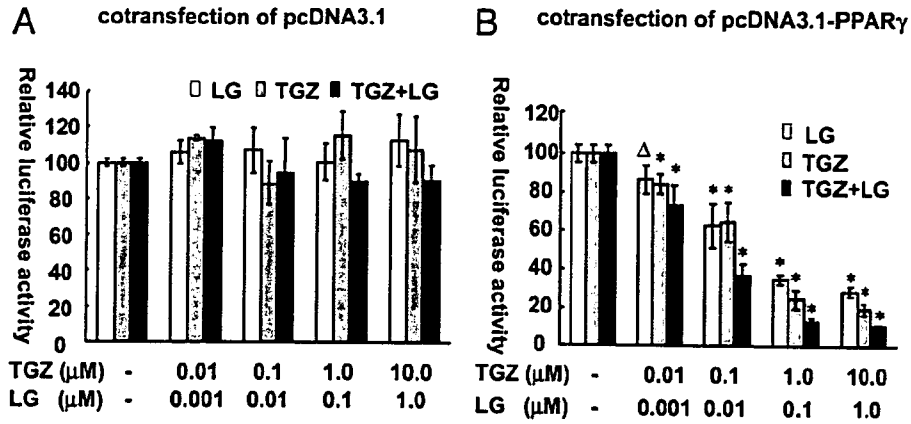

FIG. 2. TGZ+LG inhibits ArPII in a PPARγ-dependent manner. PPARγ-deficient NIH-3T3 cells were transfected with PGL3-ArPII; either a human PPARγ2 expression vector pcDNA3.1-PPARγ2 or the empty control pcDNA3.1 vector was cotransfected. Cells were then treated with TGZ, LG, or both for 24 h. Neither TGZ (or LG) alone nor TGZ+LG inhibited the promoter in the absence of PPARγ, whereas exogenous coexpression of the nuclear factor restored the inhibition. TGZ+LG synergistically inhibited the promoter in the presence of PPARγ. Δ, $P < 0.05$; *, $P < 0.01$, compared with basal level of the same treatment group.

resynthesis (31). As described above, cotransfection of PGL3-ArPII and pcDNA-PPARγ in NIH-3T3 cells allowed direct assessment of PPARγ mediation of the inhibitory effect on ArPII activity. CAPE was applied to this model to test the possible involvement of the NF-κB system in the inhibition. As shown in Fig. 3A, NIH-3T3 cells were treated with 20 μg/ml CAPE or 50% ethanol for 2 h before combined treatment with TGZ+LG, which lasted for 8 h. To gain a clearer inhibition, a second round of 2 h of CAPE plus 8 h of TGZ+LG was carried out before the cells were subjected to luciferase assay. Pretreatment of the cells with CAPE completely abolished the inhibitory effect of PPARγ activation, whereas the inhibition was still present with pretreatment with only the solvent for CAPE, 50% ethanol. A similar result was observed when CAPE was replaced by another NF-κB inhibitor, APDC (data not shown).

We next assessed whether the inhibition of aromatase activity caused by TGZ+LG also disappears on treatment with CAPE.

KGN cells were treated with CAPE in the same manner as above before aromatase activities were assayed. As shown in Fig. 3B, on pretreatment with 50% ethanol, the solvent for CAPE, TGZ+LG significantly inhibited aromatase activity, whereas once the cells were pretreated with CAPE, no decrease of aromatase activity was seen. These results indicate the mediation of NF-κB in the down-regulation of aromatase activity by TGZ+LG at the transcriptional level of promoter II.

NF-κB up-regulates ArPII

In the experiments described in Fig. 3, we noticed that on treatment of CAPE, even basal levels of both ArPII and aromatase activity were decreased, suggesting that NF-κB might be a positive regulator of aromatase gene. We tested this possibility by further experiments. As shown in Fig. 4A, cotransfection of the p65 subunit of NF-κB directly stimulated ArPII by 4-fold in NIH-3T3 cells. A similar phenomenon was observed in KGN cells (data not shown). NIK, which causes degradation of IκBα by phosphorylation of the latter at serine 176 and thus activates p65 (33), was used to specifically induce the endogenous activation of NF-κB. Figure 4B shows that PGL3-NF-κB, (positive control, contains three repeats of the NF-κB consensus elements) was augmented by NIK 2.80-fold. PGL-ArPII was also up-regulated 2.25 times by NIK. In the case of PGL3-Basic (negative control), NIK exhibited no effect.

TGZ+LG interfered with the interaction between NF-κB and ArPII

ChIP assay is a powerful technique to determine *in vivo* binding of transcription factors to target genes' promoters on

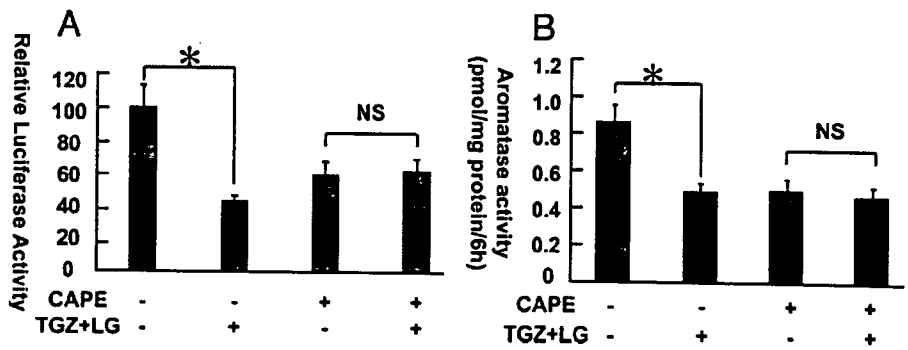

FIG. 3. TGZ+LG inhibition disappeared on NF-κB blockage. A, PGL3-ArPII was cotransfected with pcDNA3.1-PPARγ2 into NIH-3T3 cells. Cells were first treated with or without 20 μg/ml CAPE for 2 h and then with TGZ+LG or the solvent DMSO for 8 h. A second round of 2 h of CAPE (or the solvent 50% ethanol) and 8 h of TGZ+LG (or DMSO) treatment was carried out before cells were lysed for the luciferase assay. CAPE abolished the inhibitory effect of PPARγ activation and decreased the basal activity of the promoter as well. B, Aromatase activity assayed in KGN cells. Cells were treated with chemicals in the same manner as described in A. TGZ+LG inhibition of aromatase activity also disappeared on NF-κB blockage. *, $P < 0.01$; NS, not significantly different.

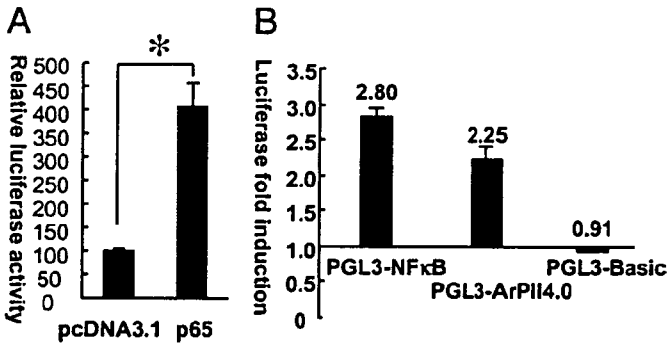

FIG. 4. NF-κB up-regulated ArPII. A, NIH-3T3 cells were transfected with PGL3-ArPII. pcDNA-p65 or pcDNA3.1 was cotransfected. ArPII activity was stimulated 4-fold by p65. B, pcDNA-NIK was transfected to NIH-3T3 cells to trigger the endogenous activation of NF-κB, whose effect on ArPII was evaluated by cotransfection of PGL3-ArPII. PGL3-NF-κB, a reporter containing three repeats of NF-κB elements, and PGL3-basic was also included as positive and negative controls, respectively. The *bars* represent the relative effect of NIK on each reporter; namely, the NIK-mediated reporter activity was divided by the control pcDNA3.1 empty vector-mediated reporter activity. *, $P < 0.01$.

chromatin. We used this assay to evaluate the interaction of NF-κB with ArPII, especially the recruitment of p65 to the promoter region. KGN cells pretreated either with an overnight 10 μM TGZ+1 μM LG or their solvent, DMSO, were challenged with 10 ng/ml TNFα or its solvent NS for 1 h before being subjected to ChIP assay with an antibody against p65. Enrichment of ArPII DNA sequences in the chromatin immunoprecipitates, which indicates association of p65 to the promoter within intact chromatin, was visualized by PCR amplification. Based on our primitive promoter deletion analysis data, which show that a 600-bp ArPII reporter already responds positively to p65 and NIK, we designed the PCR to amplify a 401-bp region of ArPII (−403 to −2, upstream of ovary exon 2, GenBank accession no. D21241). As shown in Fig. 5A, although a weak band was amplified (30 cycles) in the absence of antibody (lane 1, which may represent the nonspecific binding of the ArPII chromatin region to normal rabbit IgG), an increase in the relative intensity of ArPII PCR band amplified from samples treated with p65 antibody indicated binding between the transcription factor and the promoter (lanes 2–5). Among cells not pretreated with TGZ+LG, 1 h TNFα challenge seemed slightly increased band intensity (lane 3 *vs.* 2). Pretreatment of TGZ+LG clearly weakened the PCR band intensity (lane 4), suggesting a decreased occupancy by p65 on ArPII. However, the decrease was not observed in cells challenged with TNFα (lane 5). Control amplification was with total input DNA (Fig 5A, *lower panel*). There was no change in the amplification of input DNA in all cases.

To further objectively tell the difference between different groups of cells, we performed real-time PCR to quantify the relative amount of immunoprecipitated ArPII copies to input control for each sample. Figure 5B shows that presence of p65 antibody significantly increased the relative copy number of immunoprecipitated ArPII DNA segments, indicating that p65 associates with ArPII. And TGZ+LG pretreatment significantly reduced the relative copy number, suggesting the association was impaired. However, TNFα restored the TGZ+LG reduced relative ArPII copy number, although the cytokine did not change the copy number from cells not pretreated with TGZ+LG. Consistent with data presented in Fig. 4, these results indicated that NF-κB may interact with ArPII *in vivo*, and activation of PPARγ/RXR may interfere with the interaction.

The interference of PPARγ activation on the endogenous expression of NF-κB in KGN cells

The endogenous expression of the NF-κB system in KGN cells was tested by Western blotting, using antibodies against the p65 subunit and IκBα, and was positively controlled using NIH3T3 cells, whose endogenous NF-κB has already been proven (34). The KGN cells were treated with or without 24 h of 10 μM TGZ + 1.0 μM LG, actively lysed, and subjected to Western blotting. Figure 6 (*upper panel*) shows endogenous expression of IκBα in KGN cells and the *lower panel* the endogenous expression of the p65 subunit of NF-κB.

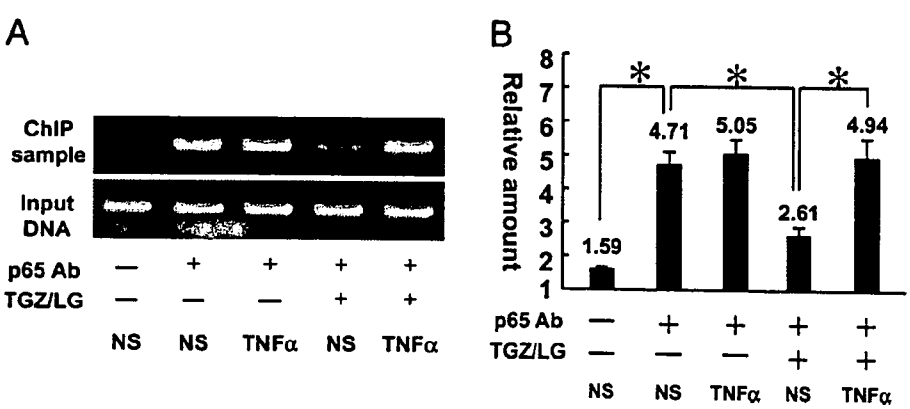

FIG. 5. ChIP assay of p65 binding to ArPII. KGN cells pretreated with or without an overnight 10.0 μM TGZ+1.0 μM LG were challenged with 10 ng/ml TNFα or its solvent, NS, for 1 h. ChIP assay was then performed with anti-p65 antibody or normal rabbit IgG as negative control. Enrichment of ArPII-specific DNA sequence in immunoprecipitated DNA pool indicating association of p65 with ArPII within intact chromatin was visualized by PCR. A, PCR was performed on immunoprecipitated DNA pool with normal rabbit IgG [p65 Ab (−)], p65 Ab, and purified input DNA (input). *Upper panel*, PCR amplified ArPII-specific bands from cells under various treatments as indicated. *Lower panel*, ArPII PCR bands from input controls. B, Real-time PCR was performed to quantify the amount of immunoprecipitated ArPII DNA copy number from cells under various treatments relative to their corresponding input controls. *, $P < 0.01$; NS, not significantly different.

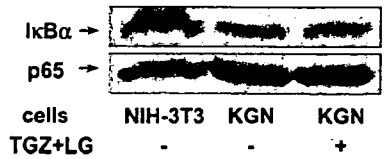

FIG. 6. TGZ+LG did not alter the endogenous expression of IκBα and p65. KGN cells were treated with 10.0 μM TGZ+1.0 μM LG for 24 h and were then subjected to Western blotting analysis for the IκBα and p65 subunits of NF-κB. NIH-3T3 cells were used as a positive control. KGN cells highly expressed both IκBα and p65, and 24 h of TGZ+LG did not apparently alter the protein expression levels.

Neither of these two proteins' expression was altered by a 24-h treatment of TGZ+LG, suggesting that PPARγ activation does not interfere with NF-κB function via down-regulation of p65 subunit expression or up-regulation of the IκB protein.

PPARγ activation suppresses NF-κB transactivation

As shown above, PPARγ activation does not apparently change the protein level of NF-κB but impairs the interaction between the transcription factor and ArPII. We subsequently studied the possible interference of PPARγ activation on NF-κB transactivation in KGN cells. As shown in Fig. 7, in KGN cells, cotransfection of 0.15 μg/well of pcDNA-p65 stimulated PGL3-NF-κB production (0.8 μg/well) approximately 4-fold, whereas the p65-augmented PGL3-NF-κB signal was decreased in a concentration-dependent manner on cotreatment with an increasing concentration of TGZ+LG. Thus, activation of PPARγ-RXR heterodimers by TGZ+LG resulted in inhibitory effects on NF-κB-mediated transcription. Namely, the final net outcome effect of PPARγ activation is a down-regulation of NF-κB transactivation activity.

Discussion

The physiological significance of the mysteriously high expression of PPARγ in ovarian granulosa cells is largely unknown. We previously reported that the synthetic PPARγ ligand, TGZ, in a concentration corresponding to human plasma TGZ concentration after oral administration of a therapeutic dosage, caused a significant decrease in aromatase activity as well as mRNA level in human ovarian granulosa cells (21). The effect was enhanced synergistically by the specific ligand (LG) for RXR, the PPARγ partner. Consistently, TGZ+LG inhibited estrogen production in KGN cells (23), and TGZ reduced estrogen levels in patients with polycystic ovary syndrome, which suggested the *in vivo* relevance of the inhibition (35). In the present study, we further demonstrated that the aromatase promoter II, which is specially used in ovary, is also inhibited by TGZ+LG, indicating that inhibition occurs at the transcriptional level. It was recently reported that 15-deoxy-$\Delta^{12,14}$ prostaglandin J2, which is believed to be the endogenous ligand for PPARγ, inhibits aromatase activity through a PPARγ-independent, but redox-sensitive, mechanism (36). However, TGZ and LG, the synthetic ligands for PPARγ and RXR, respectively, seem to exert an inhibitory function in a PPARγ-dependent way because the inhibition of ArPII could not be observed in PPARγ-deficient NIH-3T3 cells unless the nuclear receptor is exogenously expressed. It is noteworthy that even for LG-induced inhibition, PPARγ was required, suggesting that inhibition requires PPARγ-RXR heterodimers. The important involvement of PPARγ in the regulation of the aromatase gene was also strengthened by a recent report that demonstrated that an environmental toxin, a commonly used plasticizer, di-C2-ethylhexyl phthalate, decreased aromatase expression through both PPARγ and PPARα in granulosa cells (37).

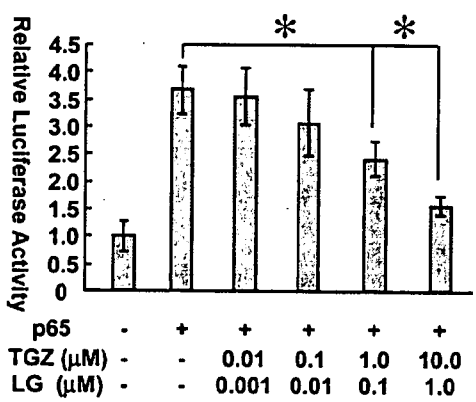

FIG. 7. TGZ+LG inhibited transactivation of NF-κB. KGN cells were transfected with PGL3-NF-κB, which contains three repeats of NF-κB elements. A p65 expression vector (pcDNA-p65) or the pcDNA3.1 empty vector was also transfected. Cells cotransfected with p65 were further treated with increasing concentrations of TGZ+LG for 24 h. TGZ+LG was shown to decrease p65-stimulated PGL3-NF-κB signal in a concentration-dependent pattern. *, $P < 0.01$.

The aromatase gene is unique in that expression of the gene in different tissues is driven by different promoters in a tissue-specific pattern (8). Promoter II is typically used to drive the gene in ovarian granulosa cells, especially before menopause. Local estrogen production in breast adipose tissue has a definite mitogenic role in breast tumors (15, 16), and local estrogen levels in breast tumors were found 10 times higher than that in the circulation of postmenopausal women (38). Although in normal adipose tissue aromatase is mainly produced via the promoter I.4 (15, 39), the local accumulation of estrogen in breast adipose tissue containing a tumor is largely due to a critical shift in promoter usage from I.4 to II (12–14, 40). In this study, we found that TGZ+LG, in a PPARγ-dependent manner, dose-dependently inhibited ArPII activity in ovarian KGN cells as well as in fibroblast NIH-3T3 cells, suggesting that the PPARγ inhibitory effect on ArPII might be universal. These data highlighted the importance of ArPII and the therapeutic potency of TGZ+LG.

Due to the lack of an apparent consensus about PPARγ-responsive element on ArPII, we hypothesized that the inhibition mechanism might be indirect (23). This idea is supported by a recent study, which shows that PPARγ is unable to bind ArPII (27).

It has been proven that the ArPII gains its maximal activity when both PKA and protein kinase C are activated by cotreatment with forskolin and tetradecanoyl phorbol acetate (41, 42). NF-κB is one of the transcriptional factors that can be activated by the activation of the protein kinase C pathway (34). Whereas on the other hand, activation of PPARγ can regulate inflammatory responses by suppressing the activation of the transcriptional factor of NF-κB (28–30). In the

present study, we tested the hypothesis that PPARγ activation may exert its inhibitory effect on ArPII by inhibiting NF-κB, which is endogenously expressed in ovarian granulosa cells and breast tissues as well (43). In this study the inhibitory effect of PPARγ-RXR activation on both ArPII and aromatase activity was found to sharply disappear on treatment with NF-κB blockers (either CAPE or APDC), suggesting that NF-κB might be the mediator of this inhibition. If this is the case, NF-κB should logically be a positive regulator of ArPII. In line with this, the basal ArPII activity as well as the aromatase activity was decreased on CAPE treatment, and activation of the NF-κB system by either forced expression of p65 or cotransfection of NIK to activate endogenous NF-κB stimulated ArPII activity. Consistently, ChIP assay also showed the interaction between NF-κB and ArPII. However, no classical consensus NF-κB-responsive element was detected on the promoter. Nevertheless, because there is an instance that NF-κB may bind a DNA motif, which is not related to the classical NF-κB consensus sequence (44), we suppose that there might exist putative ArPII-specific binding sites for p65, which are to be further delineated.

Although we observed no effect of TGZ+LG on endogenous expressions of either IκBα or p65, which is considered one possible mechanism by which NF-κB system is regulated (45). Treatment of TGZ+LG apparently weakened the interaction between p65 and ArPII, suggesting activation of PPARγ may interfere with the formation of high-order complex between NF-κB and aromatase gene at chromatin level. This is probably further explained by the finding that activated PPARγ can physically interact with p65 and results in inhibition of NF-κB (46, 47). And probably as an outcome of the impaired transcription factor-promoter association, we found that PPARγ activation by TGZ+LG suppressed the transactivation ability of NF-κB. The suppression by the PPARγ-RXR nuclear receptor system may also possibly be related to the fact that the nuclear receptors compete for limited amounts of the general coactivators, cAMP response element-binding protein and steroid receptor coactivator-1, as we previously reported (48).

Considering our previous finding that activation of a PPARγ-RXR nuclear receptor system by TGZ+LG inhibits aromatase by accelerating mRNA degradation, we report in the present study that TGZ+LG inhibited transcriptional activity of the ArPII in a PPARγ-dependent manner. These data reinforce the potential use of synthetic PPARγ and RXR agonists for therapeutic applications in diseases in which estrogens, locally or systematically, play prominent pathogenic roles, especially in diseases like breast cancer. In addition, we found that the inhibition disappeared on blockage of NF-κB, which was found in turn to positively regulate aromatase. Notably, activation of NF-κB has been found involved in the proliferation and metastasis of breast cancer cells (43), for which, although several mechanisms have been suggested, we suppose that stimulation of aromatase might be an additional one. Classically, regulation of ArPII involves PKA-cAMP response element-binding protein (49) and the orphan nuclear receptor steroidogenic factor 1 (Ad4BP/SF-1) (50), but the actual regulation may be much more complicated, at least in that nuclear receptors like PPARγ, RXR, and their cross-talk with the transcriptional factor NF-κB might also play some important roles.

Acknowledgments

Received August 10, 2004. Accepted September 20, 2004.

Address all correspondence and requests for reprints to: Toshihiko Yanase, M.D., Ph.D., Department of Medicine and Bioregulatory Science, Graduate School of Medical Science, Kyushu University, Maidashi 3-1-1, Higashi-ku, Fukuoka 812-8582, Japan. E-mail: yanase@intmed3.med.kyushu-u.ac.jp.

References

1. **Thompson Jr EA, Siiteri PK** 1974 Utilization of oxygen and reduced nicotinamide adenine dinucleotide phosphate by human placental microsomes during aromatization of androstenedione. J Biol Chem 249:5364–5372
2. **Means GD, Kilgore MW, Mahendroo MS, Mendelson CR, Simpson ER** 1991 Tissue-specific promoters regulate aromatase cytochrome P450 gene expression in human ovary and fetal tissues. Mol Endocrinol 5:2005–2013
3. **Jenkins C, Michael D, Mahendroo M, Simpson E** 1993 Exon-specific northern analysis and rapid amplification of cDNA ends (RACE) reveal that the proximal promoter II (PII) is responsible for aromatase cytochrome P450 (*CYP19*) expression in human ovary. Mol Cell Endocrinol 97:R1–R6
4. **Tsai-Morris CH, Aquilana DR, Dufau ML** 1985 Cellular localization of rat testicular aromatase activity during development. Endocrinology 116:38–46
5. **Nitta H, Bunick D, Hess RA, Janulis L, Newton SC, Millette CF, Osawa Y, Shizuta Y, Toda K, Bahr JM** 1993 Germ cells of the mouse testis express aromatase. Endocrinology 132:1396–1401
6. **Naftolin F, Ryan KJ, Davies IJ, Reddy VV, Flores F, Petro Z, Kuhn M, White RJ, Takaoka Y, Wolin L** 1975 The formation of estrogens by central neuroendocrine tissues. Recent Prog Horm Res 31:295–319
7. **Roselli CE, Horton LE, Resko JA** 1985 Distribution and regulation of aromatase activity in the rat hypothalamus and limbic system. Endocrinology 117:2471–2477
8. **Simpson ER, Michael MD, Agarwal VR, Hinshelwood MM, Bulun SE, Zhao Y** 1997 Cytochromes P450 11: expression of the *CYP19* (aromatase) gene: an unusual case of alternative promoter usage. FASEB J 11:29–36
9. **Bokhman JV** 1983 Two pathogenetic types of endometrial carcinoma. Gynecol Oncol 15:10–17
10. **Sasano H, Harada N** 1998 Intratumoral aromatase in human breast, endometrial, and ovarian malignancies. Endocr Rev 19:593–607
11. **Yue W, Wang JP, Hamilton CJ, Demers LM, Santen RJ** 1998 *In situ* aromatization enhances breast tumor estradiol levels and cellular proliferation. Cancer Res 58:927–932
12. **Agarwal VR, Bulun SE, Leitch M, Rohrich R, Simpson ER** 1996 Use of alternative promoters to express the aromatase cytochrome P450 (*CYP19*) gene in breast adipose tissues of cancer-free and breast cancer patients. J Clin Endocrinol Metab 81:3843–3849
13. **Zhou C, Zhou D, Esteban J, Murai J, Siiteri PK, Wilczynski S, Chen S** 1996 Aromatase gene expression and its exon I usage in human breast tumors. J Steroid Biochem Mol Biol 59:163–171
14. **Harada N** 1997 Aberrant expression of aromatase in breast cancer tissues. J Steroid Biochem Mol Biol 61:175–184
15. **Bulun SE, Simpson ER** 1994 Competitive reverse transcription-polymerase chain reaction analysis indicates that levels of aromatase cytochrome P450 transcripts in adipose tissue of buttocks, thighs, and abdomen of women increase with advancing age. J Clin Endocrinol Metab 78:428–432
16. **Bulun SE, Price TM, Aitken J, Mahendroo MS, Simpson ER** 1993 A link between breast cancer and local estrogen biosynthesis suggested by quantification of breast adipose tissue aromatase cytochrome P450 transcripts using competitive polymerase chain reaction after reverse transcription. J Clin Endocrinol Metab 77:1622–1628
17. **Kliewer SA, Forman BM, Blumberg B, Ong ES, Borgmeyer U, Mangelsdorf DJ, Umesono K, Evans RM** 1994 Differential expression and activation of a family of murine peroxisome proliferator-activated receptors. Proc Natl Acad Sci USA 91:7355–7359
18. **Lemberger T, Desvergne B, Wahli W** 1996 PPARs: a nuclear receptor-signaling pathway in lipid metabolism. Annu Rev Cell Dev Biol 12:335–363
19. **Tontonoz P, Hu E, Graves RA, Budavari AI, Spiegelman BM** 1994 mPPAR γ2: tissue-specific regulator of an adipocyte enhancer. Genes Dev 8:1224–1234
20. **Braissant O, Foufelle F, Scotto C, Dauca M, Wahli W** 1996 Differential expression of peroxisome proliferator-activated receptors (PPARs): tissue distribution of PPAR-α, -β, and -γ in the adult rat. Endocrinology 137:354–366
21. **Mu YM, Yanase T, Nishi Y, Waseda N, Oda T, Tanaka A, Takayanagi R, Nawata H** 2000 Insulin sensitizer, troglitazone, directly inhibits aromatase activity in human ovarian granulosa cells. Biochem Biophys Res Commun 271:710–713
22. **Komar CM, Braissant O, Wahli W, Curry Jr TE** 2001 Expression and local-

ization of PPARs in the rat ovary during follicular development and the periovulatory period. Endocrinology 142:4831–4838
23. **Mu YM, Yanase T, Nishi Y, Takayanagi R, Goto K, Nawata H** 2001 Combined treatment with specific ligands for PPARγ:RXR nuclear receptor system markedly inhibits the expression of cytochrome aromatase in human granulosa cancer cells. Mol Cell Endocrinol 181:239–248
24. **Yanase T, Mu YM, Nishi Y, Goto K, Nomura M, Okabe T, Takayanagi R, Nawata H** 2001 Regulation of aromatase by nuclear receptors. J Steroid Biochem Mol Biol 79:187–192
25. **Nishi Y, Yanase T, Mu Y, Oba K, Ichino I, Saito M, Nomura M, Mukasa C, Okabe T, Goto K, Takayanagi R, Kashimura Y, Haji M, Nawata H** 2001 Establishment and characterization of a steroidogenic human granulosa-like tumor cell line, KGN, that expresses functional follicle-stimulating hormone receptor. Endocrinology 142:437–445
26. **Tontonoz P, Hu E, Spiegelman BM** 1994 Stimulation of adipogenesis in fibroblasts by PPAR γ 2, a lipid-activated transcription factor. Cell 79:1147–1156
27. **Rubin GL, Duong JH, Clyne CD, Speed CJ, Murata Y, Gong C, Simpson ER** 2003 Ligands for the peroxisomal proliferator-activated receptor γ and the retinoid X receptor inhibit aromatase cytochrome P450 (*CYP19*) expression mediated by promoter II in human breast adipose. Endocrinology 143:2863–2871
28. **Wang N, Verna L, Chen NG, Chen J, Li H, Forman BM, Stemerman MB** 2002 Constitutive activation of peroxisome proliferator-activated receptor suppresses pro-inflammatory adhesion molecules in human vascular endothelial cells. J Biol Chem 277:34176–34181
29. **Ricote M, Li AC, Willson TM, Kelly CJ, Glass CK** 1998 The peroxisome proliferator-activated receptor-γ is a negative regulator of macrophage activation. Nature 391:79–82
30. **Jiang C, Ting AT, Seed B** 1998 PPAR-γ agonists inhibit production of monocyte inflammatory cytokines. Nature 391:82–86
31. **Natarajan K, Singh S, Burke Jr TR, Grunberger D, Aggarwal BB** 1996 Caffeic acid phenethyl ester is a potent and specific inhibitor of activation of nuclear transcription factor NF-κB. Proc Natl Acad Sci USA 93:9090–9095
32. **Fujii A, Harada T, Yamauchi N, Iwabe T, Nishi Y, Yanase T, Nawata H, Terakawa N** 2003 Interleukin-8 gene and protein expression are up-regulated by interleukin-1β in normal human ovarian cells and a granulosa tumor cell line. Fertil Steril 79:151–157
33. **Ozes ON, Mayo LD, Gustin JA, Pfeffer SR, Pfeffer LM, Donner DB** 1999 NF-κB activation by tumor necrosis factor requires the Akt serine-threonine kinase. Nature 401:82–85
34. **Diaz-Meco MT, Berra E, Municio MM, Sanz L, Lozano J, Dominguez I, Diaz-Golpe V, Lain de Lera MT, Alcami J, Paya CV** 1993 A dominant negative protein kinase Cζ subspecies blocks NF-κB activation. Mol Cell Biol 13:4770–4775
35. **Dunaif A, Scott D, Finegood D, Quintana B, Whitcomb R** 1996 The insulin-sensitizing agent troglitazone improves metabolic and reproductive abnormalities in the polycystic ovary syndrome. J Clin Endocrinol Metab 81:3299–3306
36. **Winnett G, van Hagen D, Schrey M** 2003 Prostaglandin J2 metabolites inhibit aromatase activity by redox-sensitive mechanisms: potential implications for breast cancer therapy. Int J Cancer 103:600–605
37. **Lovekamp-Swan T, Jetten AM, Davis BJ** 2003 Dual activation of PPARα and PPARγ by mono-(2-ethylhexyl) phthalate in rat ovarian granulosa cells. Mol Cell Endocrinol 201:133–141
38. **Van Landeghem AA, Poortman J, Nabuurs M, Thijssen JH** 1985 Endogenous concentration and subcellular distribution of estrogens in normal and malignant human breast tissue. Cancer Res 45:2900–2906
39. **Grodin JM, Siiteri PK, MacDonald PC** 1973 Source of estrogen production in postmenopausal women. J Clin Endocrinol Metab 36:207–214
40. **Bulun SE, Mahendroo MS, Simpson ER** 1994 Aromatase gene expression in adipose tissue: relationship to breast cancer. J Steroid Biochem Mol Biol 49:319–326
41. **Zhao Y, Agarwal VR, Mendelson CR, Simpson ER** 1996 Estrogen biosynthesis proximal to a breast tumor is stimulated by PGE2 via cyclic AMP, leading to activation of promoter II of the *CYP19* (aromatase) gene. Endocrinology 137:5739–5742
42. **Evans CT, Corbin CJ, Saunders CT, Merill JC, Simpson ER, Mendelson CR** 1987 Regulation of estrogen biosynthesis in human adipose stromal cells. Effects of dibutyryl cyclic AMP, epidermal growth factor, and phorbol esters on the synthesis of aromatase cytochrome P-450. J Biol Chem 262:6914–6920
43. **Watabe M, Hishikawa K, Takayanagi A, Shimizu N, Nakaki T** 2004 Caffeic acid phenethyl ester induces apoptosis by inhibition of NFκB and activation of Fas in human breast cancer MCF-7 cells. J Biol Chem 279:6017–6026
44. **Todorov VT, Volkl S, Muller M, Bohla A, Klar J, Kunz-Schughart LA, Hehlgans T, Kurtz A** 2004 Tumor necrosis factor-α activates NFκB to inhibit renin transcription by targeting cAMP-responsive element. J Biol Chem 279:1458–1467
45. **Delerive P, Gervois P, Fruchart JC, Staels B** 2000 Induction of IκBα expression as a mechanism contributing to the anti-inflammatory activities of peroxisome proliferator-activated receptor-α activators. J Biol Chem 275:36703–36707
46. **Chen F, Wang M, O'Connor JP, He M, Tripathi T, Harrison LE** 2003 Phosphorylation of PPARγ via active ERK1/2 leads to its physical association with p65 and inhibition of NF-κβ. J Cell Biochem 90:732–744
47. **Chung SW, Kang BY, Kim SH, Pak YK, Cho D, Trinchieri G, Kim TS** 2000 Oxidized low density lipoprotein inhibits interleukin-12 production in lipopolysaccharide-activated mouse macrophages via direct interactions between peroxisome proliferator-activated receptor-γ and nuclear factor-κB. J Biol Chem 275:32681–32687
48. **Uchimura K, Nakamuta M, Enjoji M, Irie T, Sugimoto R, Muta T, Iwamoto H, Nawata H** 2001 Activation of retinoic X receptor and peroxisome proliferator-activated receptor-γ inhibits nitric oxide and tumor necrosis factor-α production in rat Kupffer cells. Hepatology 33:91–99
49. **Michael MD, Michael LF, Simpson ER** 1997 A CRE-like sequence that binds CREB and contributes to cAMP-dependent regulation of the proximal promoter of the human aromatase P450 (*CYP19*) gene. Mol Cell Endocrinol 134:147–156
50. **Michael MD, Kilgore MW, Morohashi K, Simpson ER** 1995 Ad4BP/SF-1 regulates cyclic AMP-induced transcription from the proximal promoter (PII) of the human aromatase P450 (*CYP19*) gene in the ovary. J Biol Chem 270:13561–13566

***Endocrinology* is published monthly by The Endocrine Society (http://www.endo-society.org), the foremost professional society serving the endocrine community.**

Androgen Receptor Null Male Mice Develop Late-Onset Obesity Caused by Decreased Energy Expenditure and Lipolytic Activity but Show Normal Insulin Sensitivity With High Adiponectin Secretion

WuQiang Fan,[1] Toshihiko Yanase,[1] Masatoshi Nomura,[1] Taijiro Okabe,[1] Kiminobu Goto,[1] Takashi Sato,[2] Hirotaka Kawano,[2] Shigeaki Kato,[2] and Hajime Nawata[1]

Androgen receptor (AR) null male mice ($AR^{L-/Y}$) revealed late-onset obesity, which was confirmed by computed tomography–based body composition analysis. $AR^{L-/Y}$ mice were euphagic compared with the wild-type male ($AR^{X/Y}$) controls, but they were also less dynamic and consumed less oxygen. Transcript profiling indicated that $AR^{L-/Y}$ mice had lower transcripts for the thermogenetic uncoupling protein 1, which was subsequently found to be ligand-dependently activated by AR. We also found enhanced secretion of adiponectin, which is insulin sensitizing, from adipose tissue and a relatively lower expression of peroxisome proliferator–activated receptor-γ in white adipose tissue in comparison to $AR^{X/Y}$ mice. Both factors might explain why the overall insulin sensitivity of $AR^{L-/Y}$ mice remained intact, despite their apparent obesity. The results revealed that AR plays important roles in male metabolism by affecting the energy balance, and it is negative to both adiposity and insulin sensitivity. *Diabetes* **54:1000–1008, 2005**

The etiology of obesity is extremely heterogeneous, in that it is the final result of interactions among genetic, environmental, and psychosocial factors. The androgen receptor (AR) gene may be one of these genetic factors. AR gene repeat variation was shown to be strongly associated with central obesity indexes in older adults (1). Testosterone is an important factor for determining body composition in males. Abdominal obesity is inversely correlated with serum testosterone levels in men but not in women (2). Steady increases in body fat mass accompany the age-dependent decrease in serum testosterone levels in men (3,4), leading to greater morbidity (5). Pathologically hypogonadal men also have a significantly higher fat mass (3,6), which is reversed by testosterone administration (7,8), whereas suppression of serum testosterone in healthy young men increased the percent fat mass and decreased lipid oxidation rates and resting energy expenditure (9).

We generated an AR null (ARKO) mouse line, using a Cre-loxP system (10–12), and found that male ARKO mice ($AR^{L-/Y}$) developed late-onset obesity, whereas neither heterozygous nor homozygous female ARKO mice were affected (10), suggesting a male-specific AR effect on adiposity.

Herein we report the underlying mechanism of late-onset obesity in $AR^{L-/Y}$ mice. Despite a lack of hyperphagia, $AR^{L-/Y}$ mice had lower spontaneous activity and a decreased overall oxygen consumption ratio. We also observed a concomitant decrease in expression of the thermogenic uncoupling protein 1 (UCP-1). In addition, a unique lack of insulin resistance in $AR^{L-/Y}$ mice, despite the obese phenotype, suggests it was related to an enhanced secretion of adiponectin from adipose tissue.

RESEARCH DESIGN AND METHODS

An ARKO mutant mouse line was established and maintained as described previously (10–12). Heterozygous females were bred to wild-type males (C57BL/6NCrj; Charles River Japan, Tokyo, Japan) to produce ARKO male mice ($AR^{L-/Y}$) and heterozygous females. Their diet (CLEA rodent diet CE-2; Kyudo, Tosu, Saga, Japan) had the following composition: 54.4% carbohydrate, 24.4% protein, 4.4% fat, and 342.2 kcal/100 g. Mice were weighed weekly, and food consumption was measured by weighing the remaining food every 3 days. All animal protocols were approved by the animal care and use committee of Kyushu University.

Body fat composition analysis. For computed tomography (CT) analysis of body fat composition, mice were anesthetized with intraperitoneal injections of pentobarbital sodium (Nembutal; Dainippon Pharmaceutical, Osaka, Japan) and then scanned using a LaTheta (LCT-100M) experimental animal CT system (Aloka, Tokyo, Japan). Contiguous 2-mm slice images between L2 and L4 were used for quantitative assessment using LaTheta software (version 1.00). Visceral fat, subcutaneous fat, and muscle were distinguished and evaluated quantitatively.

Spontaneous activity. Spontaneous physical activity was measured using a Letica infrared system (Panlab, Barcelona, Spain). The mice were placed in a 45 × 45 cm^2 infrared frame in which 16 × 16 intercepting infrared light beams formed a double grid of infrared cells. The position of the mice within the infrared frame was traced in a real-time manner. An additional upper infrared frame was applied to detect rearing (mouse standing up on its hind legs). Parameters such as distance traveled, speed, rearing number, and duration were analyzed using the Acti-Track program. By setting two speed thresholds

From the [1]Department of Medicine and Bioregulatory Science, Graduate School of Medical Science, Kyushu University, Fukuoka, Japan; and the [2]Institute of Molecular and Cellular Biosciences, Graduate School of Agricultural and Life Sciences, University of Tokyo, Tokyo, Japan.

Address correspondence and reprint requests to Toshihiko Yanase, MD, PhD, Department of Medicine and Bioregulatory Science, Graduate School of Medical Science, Kyushu University, Maidashi 3-1-1, Higashi-ku, Fukuoka, 812-8582 Japan. E-mail: yanase@intmed3.med.kyushu-u.ac.jp.

Received for publication 2 September 2004 and accepted in revised form 6 January 2005.

AR, androgen receptor; BAT, brown adipose tissue; CT, computed tomography; PPAR-γ, peroxisome proliferator–activated receptor-γ; UCP, uncoupling protein; WAT, white adipose tissue.

TABLE 1
List of primers

Target	Forward	Reverse	Size
UCP-2	AACAGTTCTACACCAAGGGC	AGCATGGTAAGGGCACAGTG	471
β-Actin	GCAATGCCTGGGTACATGGTGG	GTCGTACCACAGGCATTGTGATGG	492
Acetyl CoA carboxylase	GGGACTTCATGAATTTGCTGATTCTCAGTT	GTCATTACCATCTTCATTACCTCAATCTC	728
Fatty acid synthase	CACAGATGATGACAGGAGATGG	TCGGAGTGAGGCTGGGTTGAT	205
PPAR-γ coactivator 1	CGCAGCCCTATTCATTGTTC	TCATCCCTCTTGAGCCTTTC	364
Sterol regulatory element–binding protein 1c	ATCGGCGCGGAAGCTGTCGGGGTAG	ACTGTCTTGGTTGTTGATGAGCTGGAGCA	116
Leptin	TCCAGAAAGTCCAGGATGACAC	CACATTTTGGGAAGGCAGG	212
Carnitine palmitoyl transferase 1	ATTCTGTGCGGCCCTTATTGGAT	TTTGCCTGGGATGCGTGTAGTGT	395
Long-chain acyl-CoA dehydrogenase	GCTGCCCTCCTCCCGATGTT	ATGTTTCTCTGCGATGTTGATG	258
UCP-1	CACCTTCCCGCTGGACAC	CCCTAGGACACCTTTATACCTAATG	91
Hormone-sensitive lipase	CCTACTGCTGGGCTGTCAA	CCATCTGGCACCCTCACT	142
PPAR-γ	TTGACAGGAAAGACAACGGA	GAGCAGAGTCACTTGGTCATT	246
GLUT4	TCTCCAACTGGACCTGTAAC	TCTGTACTGGGTTTCACCTC	221
Muscle-type phosphofructokinase	AGATGGGTGCTAAGGCTATG	TTTTGAGGATTGGCCTCAGC	218
Muscle-type pyruvate kinase	CATTGCCGTGACTCGAAATC	CATGGTGTTGGTGAATCCAG	225
Hexokinase I	CGTGGTGCAAAAGATCCGAG	CTGCTCTTAGGCGTTCGTAG	243
Hexokinase II	TCTCAGATCGAGAGTGACTG	CGTCTCATGCATGACTTTGG	272
AR	CAGCATTATTCCAGTGGATGG	GGGCACTTGCACAGAGATG	274
UCP-1 promoter	TCCATTGGCCTCAAACCCTATGAG	AGGCGTGAGTGCAAGAACAAAAGG	3,850

of 2.00 and 5.00 cm/s, the movements were subclassified into resting (slower than 2.00 cm/s), moving slowly (between 2.00 and 5.00 cm/s), and moving fast (faster than 5.00 cm/s). The mice were placed into the frame 5 h before commencing recording to allow familiarization with the surroundings. Recording was started 2 h after the lights were switched off and lasted for 8 h; mice were assessed individually.

Oxygen consumption measurements. Mice were fed regular chow, maintained at a constant room temperature (21–23°C), and subjected to oxygen consumption measurements at ~22 weeks of age using a computer-controlled open-circuit indirect calorimeter (Oxymax; Columbus Instruments, Columbus OH). Mice were housed individually in metabolic chambers (10 × 20 cm^2) and had free access to food and water. After a 1-h adaptation to the chamber, Vo_2 was assessed at 4-min intervals for 24 h. All sample data were analyzed using Oxymax Windows software (version 1.0).

Glucose tolerance and insulin challenge tests. For the intraperitoneal glucose tolerance test, mice were fasted overnight and then injected with 2 g D-glucose/kg body wt i.p. Tail blood glucose levels were monitored before and at 15, 30, 60, 90, and 120 min after injection using blood glucose meters (Matsushita Kotobuki Electronics Industries, Ehime, Japan). For the insulin challenge test, mice were fasted overnight and then injected with 0.7 units regular insulin/kg body wt i.p. Tail blood glucose levels were measured at the same time points as above.

Histology. Mice were killed at 45 weeks old after an overnight fast, and blood was collected by cardiac puncture. Subcutaneous white adipose tissue (WAT), interscapular brown adipose tissue (BAT), liver, and kidneys were removed and immersion-fixed in 4% paraformaldehyde. After dehydration, tissue samples were paraffin-embedded in a random orientation, sliced into 10-μm sections, and stained with hematoxylin and eosin.

Blood chemicals. Blood was collected at the time of death, and the isolated serum was aliquoted and stored at −20°C until use. All blood chemistry items were measured by SRL (Tokyo, Japan). Plasma full-length adiponectin levels were measured using an enzyme-linked immunosorbent assay system as previously described (13).

Real-time PCR. Total RNA was isolated from 100 mg of intraperitoneal WAT or interscapular BAT using an RNeasy Lipid Tissue Mini Kit (Qiagen, Valencia, CA). To remove any possible DNA contamination, on-column digestion of DNA was performed with an RNase-free DNase set (Qiagen). Then, 3 μg of total RNA was subjected to reverse transcription using SuperScript III reverse transcriptase (Invitrogen, Carlsbad, CA) primed by random primers. cDNA was then subjected to real-time PCR analysis to quantify various transcripts, using a LightCycler (Roche Diagnostics, Mannheim, Germany) according to the manufacturer's instructions, as we previously described (14). The forward/reverse primer sequences for each target transcript are shown in Table 1. β-Actin was amplified simultaneously as an internal control. The real-time PCR data for each transcript were calculated as the ratio of β-actin.

UCP-1 promoter assay. A 3.85-kb (−3,860 to −10 from the start codon) region of the mouse UCP-1 promoter was amplified by PCR using specific primers (Table 1) and KOD-Plus DNA polymerase (Toyobo, Osaka, Japan) in a T-gradient thermoblock (Biometra Biomedizinische Analytik, Gottingen, Germany), and it was subsequently cloned into the pGL3-Basic (Promega, Madison, WI) vector to construct a UCP-1–Luc reporter. Direct sequencing was then performed to validate the full-length sequence and orientation. The effect of AR on the UCP-1 promoter was analyzed in NIH-3T3-L1 adipocytes by the dual luciferase assay, as described previously (15). Briefly, 1 × 10^5 cells/well were seeded into 12-well plates, and UCP-1–Luc and pCMV-AR, or pCMX (empty vector), together with the internal control pRL-CMV vector were cotransfected into the cells by SuperFect (Qiagen). The cells were incubated in 10^{-8} mol/l dihydroxytryptamine or its solvent, ethanol, for 24 h and then lysed and subjected to the relative luciferase assay using a LUMAT LB9507 luminometer (Berthold Technologies, Bad Wildbad, Germany).

Statistical analysis. Data were expressed as the means ± SD and evaluated by Student's two-tail *t* test or ANOVA, followed by post hoc comparisons with Fisher's protected least significant difference test.

RESULTS

We previously reported that up to 10 weeks old, $AR^{L-/Y}$ mice had growth retardation compared with the male wild-type ($AR^{X/Y}$) mice, but over the next couple of weeks, their body weight caught up with and then exceeded that of $AR^{X/Y}$ mice and eventually developed into overt obesity (10). These phenomena were not observed in ARKO female mice. In the present study, we performed objective CT-based body composition analysis for mice at 40 weeks of age. Figure 1*A* shows the CT-estimated weights of the adipose tissue and muscle in the area assayed (L2–L4). Although the muscle amount was unchanged, the visceral and subcutaneous fat and total fat of $AR^{L-/Y}$ mice were significantly heavier than those of $AR^{X/Y}$ mice. Figure 1*B* shows representative CT images at the L3 level of $AR^{X/Y}$ (*left*) and $AR^{L-/Y}$ (*right*) mice. $AR^{L-/Y}$ mice had increased fat in both visceral and subcutaneous areas. Thus, increased adiposity, rather than a linear increase in body growth, accounted for the elevated body weight of $AR^{L-/Y}$ mice.

The body weight of $AR^{L-/Y}$ mice at 45 weeks of age was significantly higher than that of $AR^{X/Y}$ mice (Fig. 2*A*), and, consistent with the CT data, perirenal fat pads of $AR^{L-/Y}$ mice were clearly larger that those of $AR^{X/Y}$ mice (data not shown). Despite elevated body weight, the kidneys of

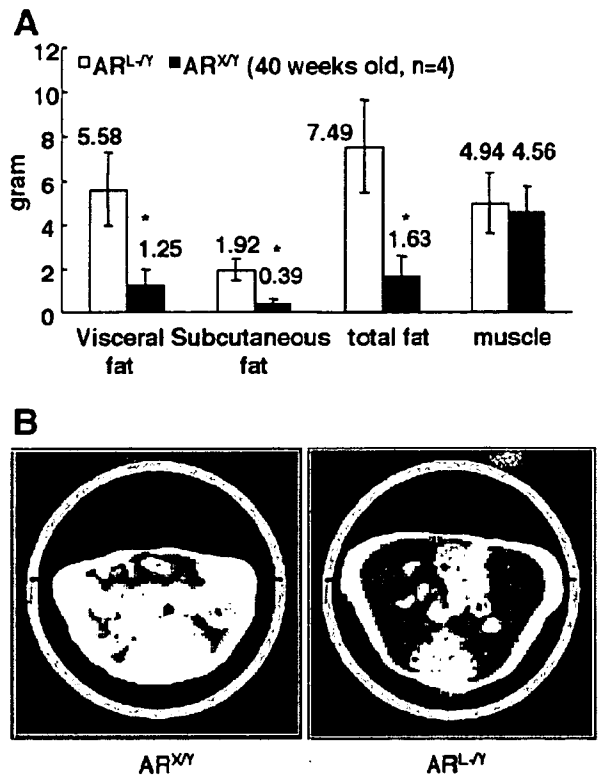

FIG. 1. CT-based body composition analysis of 40-week-old $AR^{L-/Y}$ and $AR^{X/Y}$ mice. *A*: CT-estimated amounts of visceral fat, subcutaneous fat, and muscle in the abdominal area of L2–L4. *B*: Representative CT images of $AR^{X/Y}$ (*left*) and $AR^{L-/Y}$ (*right*) mice at the L3 level. The pink and yellow areas represent the visceral and subcutaneous fat, respectively. *$P < 0.01$ compared with $AR^{L-/Y}$, $n = 4$.

$AR^{L-/Y}$ mice were significantly smaller than those of $AR^{X/Y}$ mice (Fig. 2*B*), supporting previous studies demonstrating smaller kidneys in orchidectomized mice (16,17).

In comparison to $AR^{X/Y}$ mice, subcutaneous WAT from $AR^{L-/Y}$ mice was hypertrophic (Figs. 2*C* and *D*). The interscapular BAT in $AR^{L-/Y}$ mice was relatively enlarged and pale (Fig. 2*E*), and it contained higher lipid content (Figs. 2*F* and *G*). A considerable number of cells in $AR^{L-/Y}$ BAT were large and contained unilocular lipid deposits that morphologically mimicked WAT adipocytes (data not shown). Leptin transcript, which is normally restricted to WAT, was elevated in $AR^{L-/Y}$ WAT, as expected (Fig. 2*H*). However, it was also elevated in $AR^{L-/Y}$ BAT (Fig. 2*I*), suggesting that BAT from $AR^{L-/Y}$ mice has characteristics of both BAT and WAT. Thus the BAT of $AR^{L-/Y}$ mice is similar to that from mice in which the genes encoding all three β-adrenergic receptors have been inactivated (18). Despite the apparent obesity, $AR^{L-/Y}$ mice manifested no evidence of fatty liver (data not shown), which is a common consequence of obesity. Because estrogen deficiency has been found to increase WAT in male mice (19,20), and estrogen can be produced by aromatizing testosterone (21), which is severely decreased in $AR^{L-/Y}$ mice because of atrophic testis (12), we addressed the issue of estrogen levels in $AR^{L-/Y}$ mice. We previously reported that at 8 weeks old, before the onset of obesity, serum E2 in $AR^{L-/Y}$ mice was normal (12). In the present study, we found that E2 levels in $AR^{L-/Y}$ mice at 40 weeks of age are still indistinguishable from those in $AR^{X/Y}$ mice (Fig. 2*J*), suggesting $AR^{L-/Y}$ mice are not in short supply of estrogen.

Serum levels of total protein (5.1 ± 0.61 g/dl in $AR^{X/Y}$ mice vs. 4.8 ± 0.9 g/dl in $AR^{L-/Y}$ mice, $n = 6$, $P = 0.49$), blood urea nitrogen (26.5 ± 4.6 mg/dl in $AR^{X/Y}$ vs. 20.8 ± 7.2 g/dl in $AR^{L-/Y}$ mice, $n = 6$, $P = 0.12$), and glucose (78.5 ± 14.2 mg/dl in $AR^{X/Y}$ vs. 88.0 ± 9.9 mg/dl in $AR^{L-/Y}$ mice, $n = 6$, $P = 0.26$) were found unchanged. Those of triglycerides, unesterified free fatty acids, and total cholesterol were also unchanged (10). Serum insulin in $AR^{L-/Y}$ mice tended to be slightly higher, but it did not reach statistical significance (Fig. 3*A*). Unexpectedly, we observed a significant increase in serum adiponectin concentration in $AR^{L-/Y}$ mice (Fig. 3*B*). Adiponectin sensitizes insulin sensitivity via various mechanisms (13,22), and its plasma concentration is negatively correlated with obesity. The unique hyperadiponectinemia in $AR^{L-/Y}$ mice thus prompted us to further evaluate the overall insulin sensitivity. Insulin challenge tests and intraperitoneal glucose tolerance tests were performed on 40-week-old mice. Neither test revealed any differences between the two groups (Figs. 3*C* and *D*), suggesting that overall insulin sensitivity remained intact in $AR^{L-/Y}$ mice, despite their apparent obesity. In contrast to the elevated plasma level of adiponectin, the adiponectin transcript was strikingly decreased in the WAT of obese $AR^{L-/Y}$ mice (Fig. 3*E*), as is commonly observed with obesity. The adiponectin transcript levels were found to be unchanged in $AR^{L-/Y}$ BAT (Fig. 3*F*), ruling out the possibility that BAT, though WAT-like, is an additional adiponectin source. We next carried out CT-based body composition analysis for the whole body to evaluate the relative WAT mass (%WAT) at the whole-body level (%WAT = 100% × whole-body WAT [g]/body weight [g]), and we subsequently estimated the relative total adiponectin production, using the equation: RTAP = %WAT × RAT, where RTAP is the relative total adiponectin production, and RAT is the relative adiponectin transcript copies to β-actin. As shown in Fig. 3*G*, although not statistically different, relative total adiponectin production from $AR^{L-/Y}$ mice was still lower than that from $AR^{X/Y}$ mice. Thus the discordance of adiponectin serum levels and adiponectin transcript levels in WAT still exists because serum adiponectin levels in $AR^{X/Y}$ mice were almost doubled (Fig. 3*B*). Collectively, these data suggest that the intact androgen-AR system of $AR^{X/Y}$ mice is suppressive to the secretion of adiponectin from WAT, whereas $AR^{L-/Y}$ mice had relatively enhanced secretion of the adipokine. In addition to hyperadiponectinemia, we also observed a significant reduction of peroxisome proliferator–activated receptor-γ (PPAR-γ) mRNA in the WAT of $AR^{L-/Y}$ compared with $AR^{X/Y}$ mice (Fig. 3*H*), which might also contribute to the normal insulin sensitivity of $AR^{L-/Y}$ mice (23).

We then studied the molecular events of glucose metabolism in skeletal muscle because muscle is a major target of androgen and adiponectin as well. As shown in Fig. 3*I–M*, although GLUT1 transcript levels were unchanged (data not shown), GLUT4 (muscle-dominant type) levels in $AR^{L-/Y}$ mice were significantly upregulated. The muscle-dominant hexokinase I was also upregulated, although no change was found for hexokinase II. Muscle-type phosphofructokinase tended, albeit not statistically significantly, to

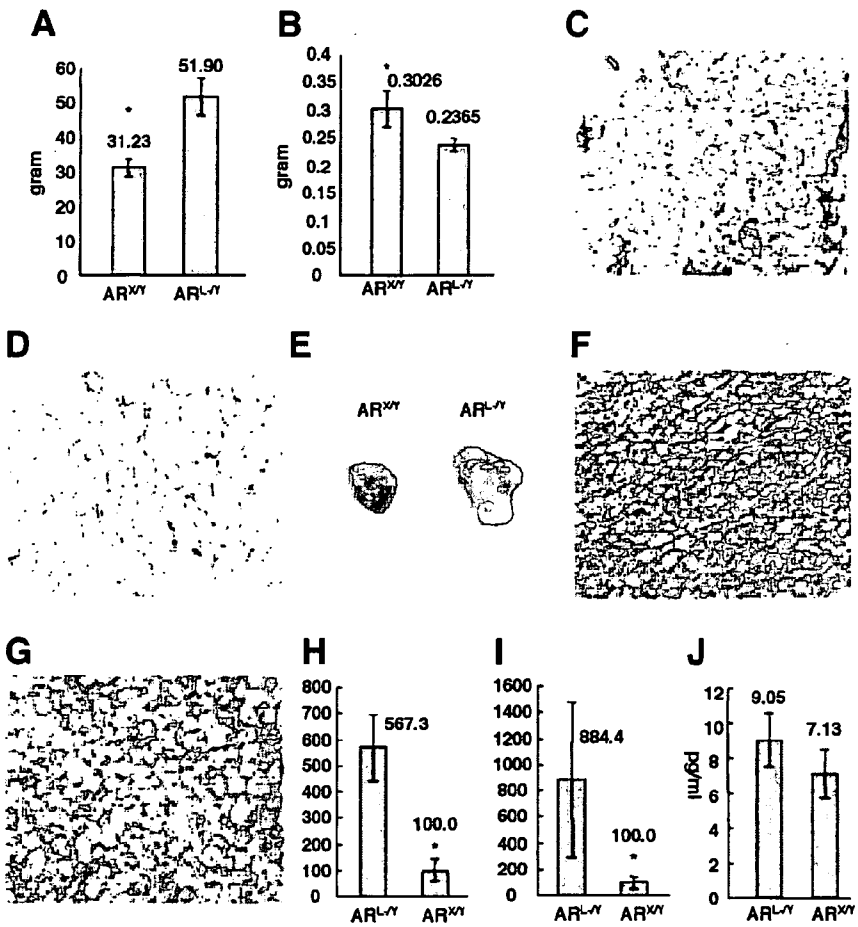

FIG. 2. General characteristics of late-onset obesity in $AR^{L-/Y}$ mice. *A*: Body weights of 45-week-old $AR^{L-/Y}$ and $AR^{X/Y}$ mice (n = 6). *B*: Kidney weights of 45-week-old $AR^{L-/Y}$ and $AR^{X/Y}$ mice (n = 6). *C* and *D*: The subcutaneous WAT of $AR^{X/Y}$ (*C*) and $AR^{L-/Y}$ mice (*D*), respectively (magnification 100×); it was hypertrophic in $AR^{L-/Y}$ compared with in $AR^{X/Y}$ mice. *E–G*: Interscapular BAT in $AR^{X/Y}$ (*F*) and $AR^{L-/Y}$ mice (*G*); it was enlarged and pale in $AR^{L-/Y}$ compared with in $AR^{X/Y}$ mice (magnification 100× in *F* and *G*). *H* and *I*: Leptin transcript levels in WAT (*H*) and BAT (*I*) in $AR^{X/Y}$ and $AR^{L-/Y}$ mice. The transcript levels in $AR^{X/Y}$ were set at 100. *J*: Serum E2 levels in $AR^{L-/Y}$ and $AR^{X/Y}$ mice. *P < 0.01 compared with $AR^{L-/Y}$ mice, n = 6.

be higher, whereas increase in muscle-type pyruvate kinase (including muscle-type pyruvate kinase-1 and -2) reached statistical significance. These data suggest glucose uptake and oxidation in muscle might be activated in $AR^{L-/Y}$ mice.

The concept of energy balance, which comprises both energy intake (feeding) and energy expenditure (physical activity, basal metabolism, and adaptive thermogenesis), is the key to understanding obesity (24). We first found that ad libitum food intake was unchanged between $AR^{L-/Y}$ and $AR^{X/Y}$ mice; that is, $AR^{L-/Y}$ mice were euphagic, as already reported (10). Next, we measured spontaneous physical activity for mice at around 8, 20, and 40 weeks of age (Table 2). During the 8-h monitoring period while the lights were off, the 20-week-old $AR^{L-/Y}$ mice ran a significantly shorter distance and showed almost half the number of rearing (standing up on hind legs) behaviors, another important parameter of dynamic behavior, as compared with $AR^{X/Y}$ mice. $AR^{L-/Y}$ mice also showed decreased activity at 40 weeks of age and, importantly, at 8 weeks of age, when the body weight of $AR^{L-/Y}$ mice had not yet exceeded that of $AR^{X/Y}$ mice. This suggests that the reduced activity of $AR^{L-/Y}$ mice is an intrinsic defect but not a secondary effect of the mice being overweight.

For the metabolic rate assessment, we first ensured that the thyroid functions of the two groups were comparable. Both serum thyrotropin (6.67 ± 3.67 ng/ml in $AR^{L-/Y}$ mice vs. 8.22 ± 2.05 ng/ml in $AR^{X/Y}$ mice, n = 6, $P > 0.05$) and 3,5,3′-triiodothyronine (0.58 ± 0.18 ng/ml in $AR^{L-/Y}$ mice versus 0.50 ± 0.11 ng/ml in $AR^{X/Y}$ mice, n = 6, $P > 0.05$) were unchanged. The rectal temperatures of both groups of mice at 22 weeks of age at room temperature were similar (37.97 ± 0.46°C in $AR^{L-/Y}$ mice vs. 38.40 ± 0.43°C in $AR^{X/Y}$ mice, $P > 0.05$). We next compared the overall oxygen consumption ratio by indirect calorimetry. To minimize interference effects of the activity differences between the two groups of mice on the Vo_2 results, we housed the mice for calorimetry in chambers of 10 × 20 cm^2, which were less than one-tenth the size of the infrared frames (45 × 45 cm^2) used to monitor the spontaneous activities. Figure 4*A* shows representative oxygen consumption (Vo_2) curves of one pair of $AR^{L-/Y}$ and $AR^{X/Y}$ mice. It is apparent that besides the average level, both peaks and troughs of the curves, which represent periods of movement and resting, respectively, are generally lower in $AR^{L-/Y}$ mice. Figure 4*B* summarizes the average mean Vo_2; $AR^{L-/Y}$ mice consumed ~30% less oxygen than $AR^{X/Y}$ mice. These data collectively indicate that $AR^{L-/Y}$ mice had a positive energy balance, which favors the onset of obesity (25). To analyze the molecular mechanisms of the increased adiposity, we applied real-time PCR to determine the transcript levels of various genes involved in thermoregulation and lipid metabolism in WAT and BAT.

In the WAT of $AR^{L-/Y}$ mice, the expression level of the most important thermogenetic molecule, UCP-1 (26), was less than one-tenth of that in $AR^{X/Y}$ mice (Fig. 5*A*). AR is possibly a novel positive regulator of the UCP-1 gene

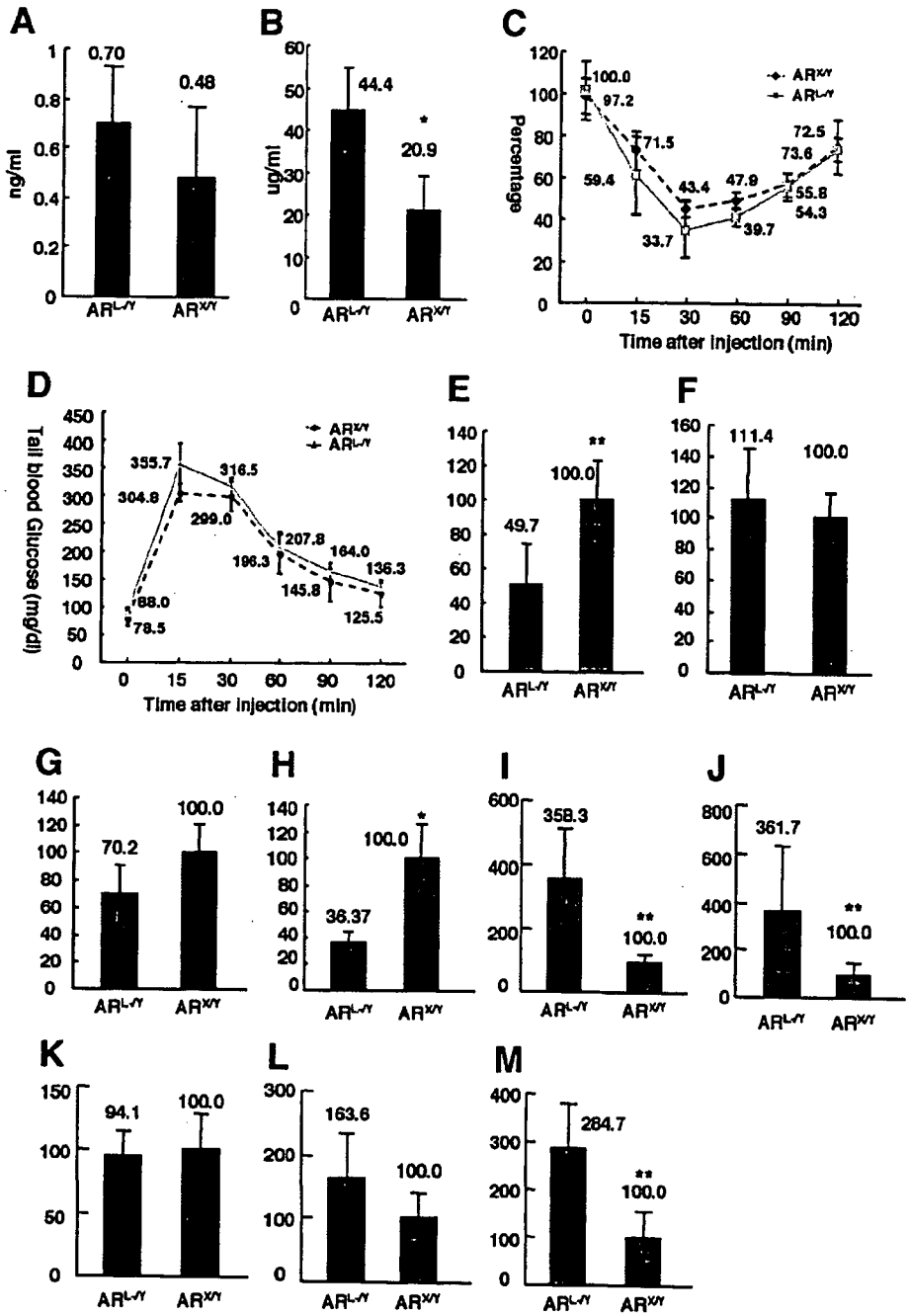

FIG. 3. Enhanced adiponectin release from WAT and intact insulin sensitivity. *A*: Serum insulin levels in $AR^{L-/Y}$ and $AR^{X/Y}$ mice. *B*: Serum adiponectin levels in $AR^{L-/Y}$ and $AR^{X/Y}$ mice. *C*: Results of the insulin challenge test; 0.7 units regular insulin/kg body wt i.p. was injected into $AR^{L-/Y}$ and $AR^{X/Y}$ mice after overnight fasting. Tail blood glucose levels were monitored at the indicated time points. The initial glucose levels in $AR^{L-/Y}$ mice were set at 100%. *D*: Results of the intraperitoneal glucose tolerance test; 2 g D-glucose/kg body wt i.p. was injected into $AR^{L-/Y}$ and $AR^{X/Y}$ mice after overnight fasting. Tail blood glucose levels were monitored at the indicated time points. Note that there was no apparent difference in overall insulin sensitivity. *E* and *F*: Transcript levels of WAT (*E*) and BAT (*F*) adiponectin in $AR^{L-/Y}$ and $AR^{X/Y}$ mice. $AR^{X/Y}$ values were set at 100. *G*: Estimated relative total adiponectin production (RTAP) in $AR^{L-/Y}$ and $AR^{X/Y}$ mice; RTAP = %WAT × RAT, where %WAT = 100% × whole-body WAT (g)/body wt (g), and RAT is the relative adiponectin transcript copies to β-actin. $AR^{X/Y}$ values were set at 100. *H*: Transcript levels of WAT PPAR-γ in $AR^{L-/Y}$ and $AR^{X/Y}$ mice. $AR^{X/Y}$ values were set at 100. *I–M*: Transcript levels of skeletal muscle GLUT4 (*I*), hexokinase I (*J*), hexokinase II (*K*), muscle-type phosphofructokinase (*L*), and muscle-type pyruvate kinase (*M*), respectively, in both groups of mice. $AR^{X/Y}$ values were set at 100. $^*P < 0.01$; $^{**}P < 0.05$ compared with $AR^{L-/Y}$ mice ($n = 6$, except *G*, in which $n = 4$).

because we revealed three steroid receptor response elements (TGTTCT) on a UCP-1 promoter sequence (up to −7,645 bp, GenBank accession no. U63418), and a 3.85-kb UCP-1 promoter, which contains the last consensus sequence, positively responded to AR in NIH-3T3-L1 adipocytes in a dihydrotestosterone-dependent manner (Fig. 5*B*). A decrease in UCP-1 transcript was also observed in the BAT of $AR^{L-/Y}$ mice (Fig. 5*C*), although it was less predominant than that in WAT; however, this is explained by the sevenfold higher expression of AR transcript in male WAT than BAT (Fig. 5*D*). The downregulation of UCP-1 might explain, to some extent, the lower V_{O_2} in

TABLE 2
Spontaneous activity at various life stages

Genotype	Body weight (g)	Distance (cm)	Speed composition			Rearing ∇ (n)	Rearing ∇ duration (s)
			% RT	% MS	% MF$^{\Delta}$		
8 weeks							
$AR^{X/Y}$	23 ± 0.69	98,816.3 ± 10,951.0	60.4	23.9	15.7	5,026.0 ± 1067.6	1.12 ± 0.23
$AR^{L-/Y}$	21 ± 1.34	66,394.8 ± 14,616.7*	72.8	17.8	9.48	2,410.5 ± 569.5*	1.20 ± 0.31
20 weeks							
$AR^{X/Y}$	31.90 ± 4.96	99,770.8 ± 27,281.6	65.8	20.9	13.3	7,003.2 ± 1575.7	1.14 ± 0.16
$AR^{L-/Y}$	41.07 ± 3.18*	60,608.8 ± 11,802.8*	72.9	19.7	7.5	3,188.5 ± 594.3*	1.06 ± 0.18
40 weeks							
$AR^{X/Y}$	35.46 ± 2.91	78,210.5 ± 23,996.3	67.4	21.4	11.2	3,497.7 ± 667.2	1.50 ± 0.24
$AR^{L-/Y}$	56.50 ± 7.83*	41,480.6 ± 7,164.4*	81.8	13.9	4.2	1,532.8 ± 409.5*	1.32 ± 0.43

*$P < 0.01$ compared with $AR^{X/Y}$ (wild-type controls), $n = 6$. ∇, rearing: mouse stands up on its hind legs. RT, resting: speed <2.00 cm/s; MS, moving slowly: speed between 2.00 and 5.00 cm/s; MF, moving fast: speed >5.00 cm/s.

$AR^{L-/Y}$ mice. In addition, another thermogenetic factor, PPAR-γ coactivator 1 (27), was also significantly decreased in both the WAT and BAT of $AR^{L-/Y}$ mice (Fig. 5*E* and *F*).

Hormone-sensitive lipase catalyzes the rate-limiting step of lipolysis in adipose tissue. The transcript level of hormone-sensitive lipase was significantly decreased in $AR^{L-/Y}$ WAT (Fig. 6*A*), whereas those for de novo lipid synthesis indicators, such as fatty acid synthase (Fig. 6*B*) and acetyl-CoA carboxylase (Fig. 6*C*) as well as the lipogenic transcriptional factor sterol regulatory element–binding protein-1c (Fig. 6*D*), were not significantly changed in both WAT and BAT (data not shown). Transcripts encoding lipoprotein lipase, the key enzyme involved in lipogenesis from circulating plasma triglyceride, were found significantly decreased in $AR^{L-/Y}$ WAT (Fig. 6*E*). The fatty acid β-oxidation markers carnitine palmitoyl transferase 1 (Fig. 6*F*) and long-chain acyl-CoA dehydrogenase (Fig. 6*G*) in $AR^{L-/Y}$ WAT showed lower trends, but they were not statistically significant. In total, decreased lipolysis rather than increased lipid synthesis might account for the increased adiposity in $AR^{L-/Y}$ mice.

DISCUSSION

Our AR null mice have neither detectable AR transcript nor protein, thus theoretically abolishing any effect of the androgens-AR system. Mirroring the increased fat mass observed in hypogonadal men, $AR^{L-/Y}$ mice have increased body weight, which is largely attributable to expanded adiposity, as indicated by both CT-based body composition analysis and anatomy. Body weights of ARKO female mice were unchanged (10), suggesting AR's effect on adiposity is specific to males. Dysfunction of the estrogen–estrogen receptor system was reported to be associated with obesity in male subjects based on the finding from both estrogen receptor-α–knockout (19) and aromatase knockout mice (20). Although we may be unable to completely exclude a possibly mixed effect on the $AR^{L-/Y}$ obese phenotype from the estrogen–estrogen receptor system, in which the function is theoretically impaired because of the shortage of the substrate for androgen-estrogen conversion in $AR^{L-/Y}$ mice, the possibility might be minor because we noticed that serum estrogen levels in $AR^{L-/Y}$ mice at both 8 weeks (12) and 40 weeks of age remain intact compared with $AR^{X/Y}$ mice, suggesting $AR^{L-/Y}$ mice are not in short supply of estrogen. In addition, supplementation of the nonaromatizable androgen dihydrotestosterone corrected fat mass increase in castrated $AR^{X/Y}$ mice but not in $AR^{L-/Y}$ mice (10), confirming that androgen actions mediated via AR has a distinct and independent adiposity-lowering effect in male subjects. Thus, our ARKO mice represent a powerful model for studying the role of the androgen-AR system in male adiposity regulation.

The direct molecular mechanism accounting for hypertrophic adipocytes and expanded WAT of $AR^{L-/Y}$ mice might rely on the altered lipid homeostasis characterized by decreased lipolysis but not increased lipogenesis. Transcripts for hormone-sensitive lipase are strikingly decreased, whereas those for lipogenetic genes (fatty acid synthase, acetyl-CoA carboxylase, sterol regulatory element–binding protein-1c, and lipoprotein lipase) are not increased (unchanged or decreased). The results are consistent with previous suggestions that androgens are lipolytic (28,29) and are very different from those of aromatase knockout mice, in which lipogenesis was found enhanced

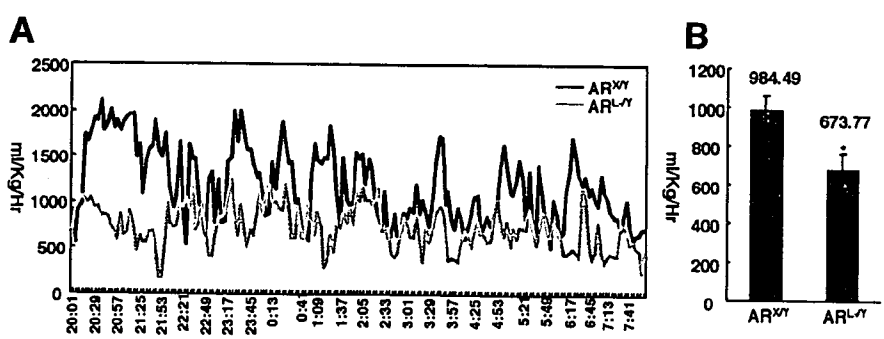

FIG. 4. Metabolic rate assessments in $AR^{L-/Y}$ and $AR^{X/Y}$ mice. *A*: Representative oxygen consumption (Vo_2) tracing curves (8 P.M. to 8 A.M.). *B*: Mean average Vo_2 values. *$P < 0.01$ compared with $AR^{X/Y}$ mice, $n = 6$.

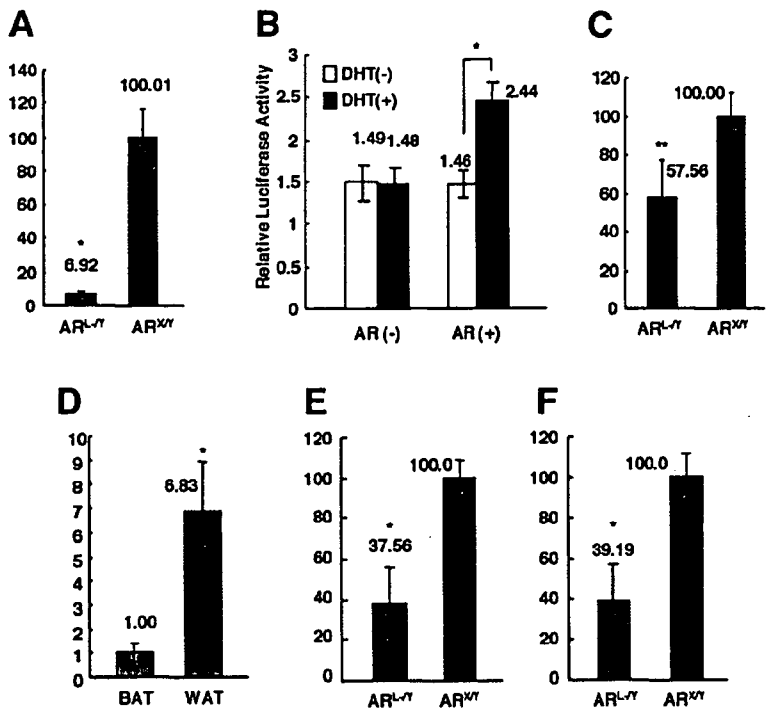

FIG. 5. Altered expressions of UCP-1. *A*: UCP-1 transcript levels in the WAT of $AR^{L-/Y}$ and $AR^{X/Y}$ mice. $AR^{X/Y}$ values were set at 100. *B*: Dual-luciferase assay of a 3.85-kb UCP-1 promoter in NIH-3T3-L1 adipocytes. In the absence of AR, dihydrotestosterone had no effect on UCP-1 promoter; however, the promoter was activated in a dihydrotestosterone-dependent manner in the presence of AR. *C*: UCP-1 transcript levels in the BAT of $AR^{L-/Y}$ and $AR^{X/Y}$ mice. $AR^{X/Y}$ values were set at 100. *D*: Relative AR transcript levels in BAT and WAT of $AR^{X/Y}$ mice. The AR transcript levels in BAT were set at 1.00. *E* and *F*: PPAR-γ coactivator 1 transcript levels in WAT (*E*) and BAT (*F*), respectively. $AR^{X/Y}$ values were set at 100. $^*P < 0.01$; $^{**}P < 0.05$ compared with $AR^{X/Y}$ mice or BAT (*D*) ($n = 6$). DHT, dihydrotestosterone.

(high lipoprotein lipase), but lipolysis was normal (30), suggesting estrogen is antilipogeneic.

Besides its negative role on adiposity, the androgen-AR system seems also to be negative to insulin sensitivity. Previous studies suggested androgen impairs insulin sensitivity in both humans and rodents (31,32). In our study, despite the obvious obese appearance, $AR^{L-/Y}$ mice reacted to both insulin and glucose challenges in manners that were indistinguishable from those of wild-type controls, indicating that the overall insulin sensitivity remained intact. This discordance between obesity and intact insulin-glucose homeostasis is unique to $AR^{L-/Y}$ mice, and it is very different from estrogen receptor-α knockout (19) or aromatase knockout (20) mice, which are accompanied by glucose intolerance and insulin resistance. One possible mechanism for the discordance might be hyperadiponectinemia. Adiponectin, originating from adipose tissue specifically, functions as an important insulin sensitizer (13,33) and correlates negatively with fat mass in that its plasma levels or adipose tissue mRNA levels decrease among obese subjects and recover after weight loss (34). The significant reduction of adiponectin transcripts in the WAT of obese $AR^{L-/Y}$ mice matches this conventional concept and thus suggests that downregula-

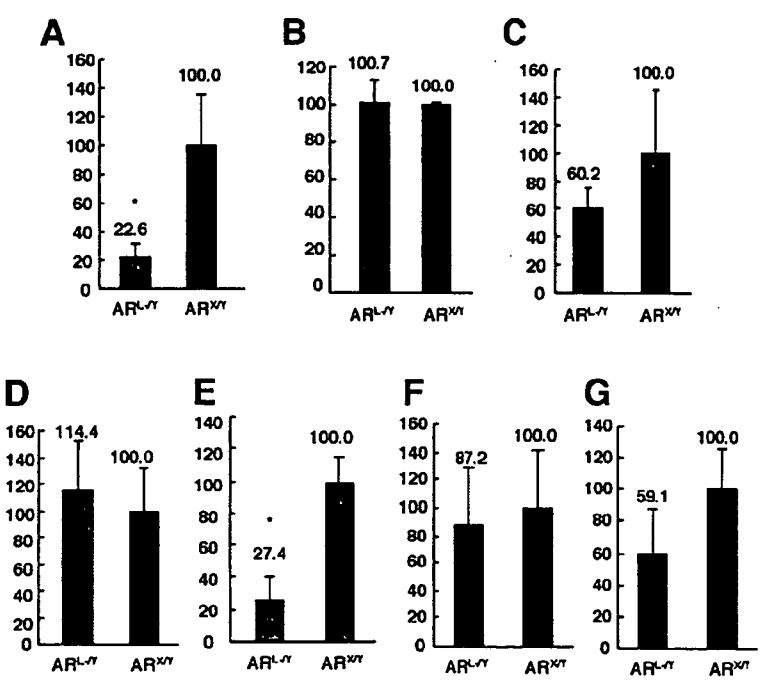

FIG. 6. WAT transcripts levels for genes involved in lipid homeostasis. *A*: Hormone-sensitive lipase transcript levels in WAT of $AR^{L-/Y}$ and $AR^{X/Y}$ mice. *B*: Fatty acid synthase transcript levels. *C*: Acetyl-CoA carboxylase transcript levels. *D*: Sterol regulatory element-binding protein 1c transcript levels. *E*: Lipoprotein lipase transcript levels. *F*: Carnitine palmitoyl transferase 1 transcript levels. *G*: Long-chain acyl-CoA dehydrogenase transcript levels. Transcripts levels in WAT of $AR^{X/Y}$ mice were set at 100. $^*P < 0.01$ compared with $AR^{X/Y}$ mice ($n = 6$).

tion happens at the transcriptional level. However, despite the lower mRNA level in WAT tissue, the serum protein level was surprisingly elevated, even after adjustment of WAT mass, indicating that the secretion process of adiponectin protein from WAT is relatively enhanced by AR inactivation. This supports a previous suggestion that testosterone inhibits adiponectin secretion from adipocytes (35,36). Thus, the androgen-AR system is an inhibitory player in the adiponectin secretion mechanism, which is largely unclarified. The inhibitory effect may also help explain the severe insulin resistance and hypoadiponectinemia observed in diseases with androgen excess, such as polycystic ovary syndrome, in which an AR blocker was found able to improve metabolic abnormalities and dysadipocytokinemia (37). Besides hyperadiponectinemia, the low expression of PPAR-γ in $AR^{L-/Y}$ WAT may also contribute to the unexpectedly normal insulin sensitivity because an intermediate level of PPAR-γ expression in WAT is the best condition for insulin sensitivity, as suggested by the finding that heterozygous PPAR-γ–deficient mice were protected from developing insulin resistance compared with wild-type mice (23).

The molecular events behind the intact glucose homeostasis, glucose uptake, and oxidation were found enhanced in skeletal muscle by AR inactivation, mirroring the clinical picture of polycystic ovary syndrome patients, where androgen excess is related with insulin resistance (32) and impaired glucose uptake (38). However, at this moment, we're not sure whether the enhanced glucose uptake and oxidation is caused directly by androgen-AR system inactivation or is secondary to hyperadiponectinemia or low PPAR-γ expression.

Body weight and the storage of energy as triglycerides in adipose tissue are homeostatically regulated by the long-term balance between energy intake and expenditure; obesity only develops if energy intake chronically exceeds the total energy expenditure (24). Although it doesn't affect appetite, AR inactivation causes an intrinsic decrease of spontaneous physical activity in male mice as well as overall oxygen consumption (Vo_2). Thus, androgen-AR system inactivation in male mice causes a chronic positive energy balance, which favors acceleration of fat mass and obesity.

In agreement with the lower Vo_2, both the thermogenic UCP-1 and PPAR-γ coactivator 1 transcripts were decreased in the adipose tissues of $AR^{L-/Y}$ mice. UCP-1, which uncouples energy substrate oxidation from mitochondrial ATP production and hence results in a loss of potential energy as heat, is one of the most important molecules responsible for adaptive thermogenesis (26). To our knowledge, this is the first time it has been shown that AR, upon its ligand binding, directly activates UCP-1 transcription, presumably by binding to the steroid response elements on the promoter.

Although AR directly regulates factors in the peripheral tissues involved in energy homeostasis, like UCP-1, it also very likely affects the mechanism exerted by the central nervous system because AR was found densely expressed in various hypothalamic nuclei, including the ventromedial hypothalamus and dorsomedial hypothalamus and the arcuate nucleus (39). The androgen-activating 5α-reductase is also expressed in the hypothalamus (40). The physiological role of the androgen-AR system in the hypothalamus is largely unknown. It is highly possible that the receptor may be involved in regulating the leptin-regulated melanocortin circuit because AR activation in the hypothalamus increases the inhibitory neuropeptide somatostatin (41,42), which may in turn inhibit the anorexigenic melanocyte-stimulating hormone or cocaine- and amphetamine-regulated transcript. The altered energy balance in $AR^{L-/Y}$ characterized by lower Vo_2 and lower physical activity warrants further study of the intra–central nervous system role of AR, which is now ongoing.

In summary, the androgen-AR system is correlated with male adiposity, and inactivation of the system causes late-onset obesity in male mice because of altered energy balance, since the $AR^{L-/Y}$ mice were euphagic but less physically dynamic and less oxygen-consuming compared with $AR^{X/Y}$ mice. The mechanism of decreased energy expenditure might reside in both the central nervous system and peripheral tissues. Besides its negative role in adiposity, the androgen-AR system also plays a negative role in insulin sensitivity, at least in part through inhibiting the release of adiponectin from adipose tissue.

ACKNOWLEDGMENTS

This work was supported in part by a grant for the 21st Century COE Program from the Japanese Ministry of Education, Culture, Sports, Science, and Technology.

REFERENCES

1. Gustafson DR, Wen MJ, Koppanati BM: Androgen receptor gene repeats and indices of obesity in older adults. *Int J Obes Relat Metab Disord* 27:75–81, 2003
2. Jorgensen JO, Vahl N, Hansen TB, Fisker S, Hagen C, Christiansen JS: Influence of growth hormone and androgens on body composition in adults. *Horm Res* 45:94–98, 1996
3. Vermeulen A: Andropause. *Maturitas* 34:5–15, 2000
4. Kyle UG, Genton L, Hans D, Karesgard L, Slosman DO, Pichard C: Age-related differences in fat-free mass, skeletal muscle, body cell mass and fat mass between 19 and 94 years. *Eur J Clin Nutr* 55:663–672, 2001
5. Matsumoto AM: Andropause: clinical implications of the decline in serum testosterone levels with aging in men. *J Gerontol A Biol Sci Med Sci* 57:M76–M99, 2002
6. Katznelson L, Rosenthal DI, Rosol MS, Anderson EJ, Hayden DL, Schoenfeld DA, Klibanski A: Using quantitative CT to assess adipose distribution in adult men with acquired hypogonadism. *Am J Roentgenol* 170:423–427, 1998
7. Rolf C, von Eckardstein S, Koken U, Nieschlag E: Testosterone substitution of hypogonadal men prevents the age-dependent increases in body mass index, body fat and leptin seen in healthy ageing men: results of a cross-sectional study. *Eur J Endocr* 146:505–511, 2002
8. Wang C, Swedloff RS, Iranmanesh A, Dobs A, Snyder PJ, Cunningham G, Matsumoto AM, Weber T, Berman N: Transdermal testosterone gel improves sexual function, mood, muscle strength, and body composition parameters in hypogonadal men. *J Clin Endocrinol Metab* 85:2839–2853, 2000
9. Mauras N, Hayes V, Welch S, Rini A, Helgeson K, Dokler M, Veldhuis JD, Urban RJ: Testosterone deficiency in young men: marked alterations in whole body protein kinetics, strength, and adiposity. *J Clin Endocrinol Metab* 83:1886–1992, 1998
10. Sato T, Matsumoto T, Yamada T, Watanabe T, Kawano H, Kato S: Late onset of obesity in male androgen receptor-deficient (AR KO) mice. *Biochem Biophys Res Commun* 300:167–171, 2003
11. Sato T, Matsumoto T, Kawano H, Watanabe T, Uematsu Y, Sekine K, Fukuda T, Aihara K, Krust A, Yamada T, Kato S: Brain masculinization requires androgen receptor function. *Proc Natl Acad Sci U S A* 101:1673–1678, 2004
12. Kawano H, Sato T, Yamada T, Matsumoto T, Sekine K, Watanabe T, Nakamura T, Fukuda T, Yoshimura K, Yoshizawa T, Kato S: Suppressive function of androgen receptor in bone resorption. *Proc Natl Acad Sci USA* 100:9416–9421, 2003

13. Maeda N, Shimomura I, Kishida K, Nishizawa H, Matsuda M, Nagaretani H, Furuyama N, Kondo H, Takahashi M, Arita Y, Komuro R, Ouchi N, Kihara S, Tochino Y, Okutomi K, Horie M, Takeda S, Aoyama T, Funahashi T, Matsuzawa Y: Diet-induced insulin resistance in mice lacking adiponectin/ACRP30. *Nat Med* 8:731–737, 2002
14. Fan W, Yanase T, Morinaga H, Mu YM, Nomura M, Okabe T, Goto K, Harada N, Nawata H: Activation of peroxisome proliferator-activated receptor-gamma and retinoid X receptor inhibits aromatase transcription via nuclear factor-kappaB. *Endocrinology* 146:85–92, 2005
15. Fan W, Yanase T, Wu Y, Kawate H, Saitoh M, Oba K, Nomura M, Okabe T, Goto K, Yanagisawa J, Kato S, Takayanagi R, Nawata H: Protein kinase A potentiates adrenal 4 binding protein/steroidogenic factor 1 transactivation by reintegrating the subcellular dynamic interactions of the nuclear receptor with its cofactors, general control nonderepressed-5/transformation/transcription domain-associated protein, and suppressor, dosage-sensitive sex reversal-1: a laser confocal imaging study in living KGN cells. *Mol Endocrinol* 18:127–141, 2004
16. Broulik PD, Schreiber V: Effect of alloxan diabetes on kidney growth in intact and castrated mice. *Acta Endocrinol* 99:109–111, 1982
17. Avdalovic N, Bates M: The influence of testosterone on the synthesis and degradation rate of various RNA species in the mouse kidney. *Biochim Biophys Acta* 407:299–307, 1975
18. Bachman ES, Dhillon H, Zhang CY, Cinti S, Bianco AC, Kobilka BK, Lowell BB: betaAR signaling required for diet-induced thermogenesis and obesity resistance. *Science* 297:843–845, 2002
19. Heine PA, Taylor JA, Iwamoto GA, Lubahn DB, Cooke PS: Increased adipose tissue in male and female estrogen receptor-alpha knockout mice. *Proc Natl Acad Sci U S A* 97:12729–12734, 2000
20. Jones ME, Thorburn AW, Britt KL, Hewitt KN, Wreford NG, Proietto J, Oz OK, Leury BJ, Robertson KM, Yao S, Simpson ER: Aromatase-deficient (ArKO) mice have a phenotype of increased adiposity. *Proc Natl Acad Sci U S A* 97:12735–12740, 2000
21. Simpson ER, Davis SR: Another role highlighted for estrogens in the male: sexual behavior. *Proc Natl Acad Sci U S A* 97:14038–14040, 2000
22. Combs TP, Berg AH, Philipp SB, Scherer E, Rossetti L: Endogenous glucose production is inhibited by the adipose-derived protein Acrp30. *J Clin Invest* 108:1875–1881, 2001
23. Kubota N, Terauchi Y, Miki H, Tamemoto H, Yamauchi T, Komeda K, Satoh S, Nakano R, Ishii C, Sugiyama T, Eto K, Tsubamoto Y, Okuno A, Murakami K, Sekihara H, Hasegawa G, Naito M, Toyoshima Y, Tanaka S, Shiota K, Kitamura T, Fujita T, Ezaki O, Aizawa S, Kadowaki T: PPAR gamma mediates high-fat diet-induced adipocyte hypertrophy and insulin resistance. *Mol Cell* 4:597–609, 1999
24. Spiegelman BM, Flier JS: Obesity and the regulation of energy balance. *Cell* 104:531–543, 2001
25. Lowell BB, Spiegelman BM: Towards a molecular understanding of adaptive thermogenesis. *Nature* 404:652–660, 2000
26. Argyropoulos G, Harper ME: Uncoupling proteins and thermoregulation. *J Appl Physiol* 92:2187–2198, 2002
27. Puigserver P, Spiegelman BM: Peroxisome proliferator-activated receptor-gamma coactivator 1 alpha (PGC-1 alpha): transcriptional coactivator and metabolic regulator. *Endocr Rev* 24:78–90, 2003
28. Xu X, De Pergola G, Bjorntorp P: The effects of androgens on the regulation of lipolysis in adipose precursor cells. *Endocrinology* 126:1229–1234, 1990
29. Sih R, Morley JE, Kaiser FE, Perry III HM, Patrick P, Ross C: Testosterone replacement in older hypogonadal men: a 12-month randomized controlled trial. *J Clin Endocrinol Metab* 82:1661–1667, 1997
30. Misso ML, Murata Y, Boon WC, Jones ME, Britt KL, Simpson ER: Cellular and molecular characterization of the adipose phenotype of the aromatase-deficient mouse. *Endocrinology* 144:1474–1480, 2003
31. Shoupe D, Lobo RA: The influence of androgens on insulin resistance. *Fertil Steril* 41:385–388, 1984
32. Toprak S, Yonem A, Cakir B, Guler S, Azal O, Ozata M, Corakci A: Insulin resistance in nonobese patients with polycystic ovary syndrome. *Horm Res* 55:65–70, 2001
33. Yamauchi T, Kamon J, Waki H, Imai Y, Shimozawa N, Hioki K, Uchida S, Ito Y, Takakuwa K, Matsui J: Globular adiponectin protected ob/ob mice from diabetes and ApoE-deficient mice from atherosclerosis. *J Biol Chem* 278:2461–2468, 2003
34. Pittas AG, Joseph NA, Greenberg AS: Adipocytokines and insulin resistance. *J Clin Endocrinol Metab* 89:447–452, 2004
35. Nishizawa H, Shimomura I, Kishida K, Maeda N, Kuriyama H, Nagaretani H, Matsuda M, Kondo H, Furuyama N, Kihara S, Nakamura T, Tochino Y, Funahashi T, Matsuzawa Y: Androgens decrease plasma adiponectin, an insulin-sensitizing adipocyte-derived protein. *Diabetes* 51:2734–2741, 2002
36. Lanfranco F, Zitzmann M, Simoni M, Nieschlag E: Serum adiponectin levels in hypogonadal males: influence of testosterone replacement therapy. *Clin Endocrinol (Oxf)* 60:500–507, 2004
37. Ibanez L, Valls C, Cabre S, De Zegher F: Flutamide-metformin plus ethinylestradiol-drospirenone for lipolysis and antiatherogenesis in young women with ovarian hyperandrogenism: the key role of early, low-dose flutamide. *J Clin Endocrinol Metab* 89:4716–4720, 2004
38. Holte J: Polycystic ovary syndrome and insulin resistance: thrifty genes struggling with over-feeding and sedentary life style? *J Endocrinol Invest* 21:589–601, 1998
39. Herbison AE: Neurochemical identity of neurones expressing oestrogen and androgen receptors in sheep hypothalamus. *J Reprod Fertil Suppl* 49:271–283, 1995
40. Poletti A, Martini L: Androgen-activating enzymes in the central nervous system. *J Steroid Biochem Mol Biol* 69:117–122, 1999
41. Zeitler P, Vician L, Chowen-Breed JA, Argente J, Tannenbaum GS, Clifton DK, Steiner RA: Regulation of somatostatin and growth hormone-releasing hormone gene expression in the rat brain. *Metabolism* 39:46–49, 1990
42. Hasegawa O, Sugihara H, Minami S, Wakabayashi I: Masculinization of growth hormone (GH) secretory pattern by dihydrotestosterone is associated with augmentation of hypothalamic somatostatin and GH-releasing hormone mRNA levels in ovariectomized adult rats. *Peptides* 13:475–481, 1992

Available online at www.sciencedirect.com

SCIENCE DIRECT

Biochimica et Biophysica Acta 1728 (2005) 84–94

BIOCHIMICA ET BIOPHYSICA ACTA
BBA

http://www.elsevier.com/locate/bba

Dehydroepiandrosterone negatively regulates the p38 mitogen-activated protein kinase pathway by a novel mitogen-activated protein kinase phosphatase

Kenji Ashida, Kiminobu Goto, Yue Zhao, Taijiro Okabe, Toshihiko Yanase, Ryoichi Takayanagi, Masatoshi Nomura, Hajime Nawata*

Department of Medicine and Bioregulatory Science (3rd Department of Internal Medicine), Graduate School of Medical Sciences, Kyushu University, Maidashi 3-1-1, Higashi-ku, Fukuoka 812-8582, Japan

Received 10 May 2004; received in revised form 10 January 2005; accepted 26 January 2005

Abstract

Dehydroepiandrosterone-sulfate, the sulfated form of dehydroepiandrosterone, is the most abundant steroid in young adults, but gradually declines with aging. In humans, the clinical application of dehydroepiandrosterone targeting some collagen diseases, such as systemic lupus erythematosus, as an adjunctive treatment has been applied in clinical trial. Here, we report that dehydroepiandrosterone may negatively regulate the mitogen-activated protein kinase pathway in humans via a novel dual specificity protein phosphatase, DDSP (dehydroepiandrosterone-enhanced dual specificity protein phosphatase). DDSP is highly homologous to LCPTP/HePTP, a tissue-specific protein tyrosine phosphatase (PTP) which negatively regulates both ERK and p38-mitogen-activated protein kinase, and is transcribed from the PTPN7 locus by alternative splicing. Although previous reports have shown that the mRNA expression of the LCPTP/HePTP gene was inducible by extracellular signals such as T-cell antigen receptor stimulation, reverse transcribed (RT)-PCR experiments using specific sets of primers suggested that the expression of LCPTP/HePTP was constitutive while the actual inducible sequence was that of DDSP. Furthermore DDSP was widely distributed among different types of human tissues and specifically interacted with p38-mitogen-activated protein kinase. This inducible negative regulation of the p38-mitogen-activated protein kinase-dependent pathway may help to clarify the broad range of dehydroepiandrosterone actions, thereby aiding the development of new preventive or adjunctive applications for human diseases.

Keywords: Dehydroepiandrosterone; Dual specificity protein phosphatase; Protein tyrosine phosphatase; p38-mitogen-activated protein kinase; Mitogen-activated protein kinase; Mitogen-activated protein kinase phosphatase

1. Introduction

The mitogen-activated protein kinase (MAPK) family plays a central role in signaling pathways stimulated by extracellular stimuli such as growth factors, cytokines and physical stress. In higher organisms, this kinase family includes the extracellular stimulus-regulated kinases (ERKs) and two stress-stimulated kinase groups, the stress-activated protein kinase/c-JUN N-terminus kinase (SAPK/JNK) and p38-MAPK/p38 High Osmolarity Glycerol response (HOG) 1 [1–5]. The activation of MAPKs requires phosphorylation of conserved tyrosine and threonine residues within the catalytic domain. This phosphorylation is mediated by dual

Abbreviations: RT-PCR, reverse transcribed PCR; MAPK, mitogen-activated protein kinase; PTP, protein tyrosine phosphatase; DSP, protein dual specificity phosphatase; LCPTP, leukocyte-specific protein tyrosine phosphatase; HePTP, hematopoietic tissue-specific protein tyrosine phosphatase; DHEA, dehydroepiandrosterone; DDSP, dehydroepiandrosterone-induced protein dual specificity phosphatase; ERK, extracellular stimulus-regulated kinase; JNK, c-*Jun* N-terminus kinase; TcR, T-cell antigen receptor; GFP, green fluorescence protein; PMA, phorbol-12-myristate-13-acetate; aa, amino acid; SSH, suppression subtraction hybridization

* Corresponding author. Tel.: +81 92 642 5275; fax: +81 92 642 5297.
E-mail address: nawata@intmed3.med.kyushu-u.ac.jp (H. Nawata).

0167-4781/$ - see front matter © 2005 Elsevier B.V. All rights reserved.
doi:10.1016/j.bbaexp.2005.01.016

specificity protein kinases, members of the MAPK kinase family. In contrast, in the absence of a signal the constituents of the MAPK cascade return to their inactive dephosphorylated state, suggesting an essential role for protein phosphatases in the negative regulation of the MAPK cascade. Protein phosphatases are classified into three groups, protein serine/threonine phosphatases, protein tyrosine phosphatases (PTPs) and protein dual specificity serine/threonine/tyrosine phosphatases (DSPs), depending on their phosphoamino acid specificity [6].

Dehydroepiandrosterone-sulfate (DHEA-S), the sulfated form of DHEA, is the most abundant steroids in young adults, but gradually decline with aging. Although the molecular basis of DHEA action still remains to be elucidated, recent findings have suggested modulatory actions of DHEA on the MAPK signal transduction pathway [7–9]. To date, much data have been accumulated on the biological action of DHEA, although some of these were carried out using rodents in which the P450 C17 activities are extremely low, thus leading to trace or nearly undetectable levels of serum DHEA or DHEAS concentrations. In humans, the clinical application of DHEA targeting hormone replacement therapy [10–13] has been tested in clinical trials.

We have been interested in the actions of DHEA using both in vitro and in vivo experiments [14] (for review). We have previously reported that a human clonal T lymphocyte, the PEER cell [15], which is stimulated with phorbol-12-myristate-13-acetate (PMA) and calcium ionophore A23187 to mimic the activation of the T-cell antigen receptor (TcR), revealed the specific binding of [3H]-DHEA to its putative receptor. This specific binding was further increased when treated with 100 nM of DHEA itself in addition to the PMA and A23187 treatment [16], while the subcellular localization of the DHEA-bound molecule(s) was not determined. In the experiment, the MAPK cascade was activated by PMA, which bypasses all receptor-induced proximal tyrosine phosphorylation events by directly activating the Raf kinase through protein kinase C [17,18]. Thus, PEER cells are likely to provide a good model for investigating the cellular phenotypes altered by the DHEA action on the MAPK cascade, or for identifying the putative receptor for DHEA. Here, we report that DHEA negatively regulates the MAPK pathway in humans via a novel MAPK phosphatase, tentatively named DDSP (DHEA-enhanced DSP), which is highly homologous to LCPTP/HePTP [19,20] not only controlling the activity of MAPKs but also mediating crosstalk between the cAMP system and the MAPK cascade [21].

2. Materials and methods

2.1. Cells

Human T lymphoblastic leukemic cells, PEER, were maintained in RPMI 1640 (Gibco) supplemented with 10% FBS, 60 μg/ml of benzylpenicillin, 100 μg/ml of streptomycin, 2 mmol/L of L-glutamine, and 50 μmol/L of 2-mercaptoethanol. The cells were plated at a concentration of 1×10^5/ml and then treated with 5 nM PMA and 500 ng/ml of calcium ionophore A23187 in the presence or absence of 50 to 100 nM of DHEA (PEER(+) and PEER(−), respectively) for 28 h. NIH3T3 mouse fibroblasts were maintained in DMEM (Gibco) supplemented with 10% FBS, 60 μg/ml of benzylpenicillin, 100 μg/ml of streptomycin, and 2 mmol/L of L-glutamine.

2.2. Suppression subtractive hybridization screening and reverse transcribed-PCR (RT-PCR)

Total RNA was isolated using ISOGEN (Nippon Gene Co.). Suppression subtraction hybridization (SSH) was performed to construct a subtraction cDNA library using a commercially available kit (PCR-Select cDNA Subtraction Kit, Clonetech Laboratories Inc.). Briefly, double-stranded cDNAs were synthesized using the poly(A)$^+$RNAs from PEER(+) or PEER(−) cells. After the completion of two rounds of hybridization, the suppression PCR products were amplified using the GeneAmp 9600 PCR System (Perkin Elmer Applied Biosystems Division), size-fractionated using Chroma Spin+TE-200 Columns (Clontech Laboratories Inc.) and then blunt ligated into pBluescript II SK−—which was cleaved with *Sma*I. DH5α was transformed with the ligation mixtures to construct the plasmid library without amplification.

The nucleotide sequences of 400 randomly chosen clones were determined using a DSQ-1000 DNA Sequencer (Shimadzu Co) and subjected to a homology search. PCR primers of 16-mers specific for the nucleotide sequence of each clone were synthesized and used for RT-PCR to confirm the effect of the DHEA treatment. Semiquantitative RT-PCR was performed using total RNAs from untreated PEER cells, PEER(+) and PEER(−) cells. The PCR fragments were electrophoresed in a 4% polyacrylamide gel. The gels were stained with Cyber Green (Amersham Life Science) and the intensities of the fluorescent signals were analyzed directly using a STORM 860 Image Analyzer (Molecular Dynamics Inc.). A phage cDNA library using the mRNAs from PEER (+) cells was constructed using a ZAP-cDNA Synthesis Kit (Stratagene) and then probed with a clone 1–20 cDNA insert. Thereafter, 1×10^6 plaques were subjected to screening.

2.3. Phosphatase assay

The full-length cDNA sequence of DDSP was ligated into the pAcGHLT baculovirus expression vector (Pharmingen), containing a 6× histidine tag and a glutathione *S*-transferase (GST) tag upstream of the multiple cloning sites, and then transfected into SF-9 (*Spodoptera frugiperda* pupal ovary) insect cells using the calcium phosphate precipitation method. Cells were grown at 25 °C and the viruses were enriched according to the manufacturer's protocol. The expressed GST-DDSP protein was purified using a glutathione sepharose affinity column. Phosphatase assays were performed using the Tyrosine Phosphatase Assay System and the Serine/Threonine Phosphatase Assay System (Promega Co.).

2.4. Tissue distribution and hormonal regulation of DDSP mRNA

The tissue distribution and hormonal regulation of DDSP or LCPTP/HePTP mRNA were examined by semiquantitative RT-

PCR. To compare the tissue distribution and steroid hormone-specific mRNA induction between DDSP and LCPTP/HePTP, 2 sets of primers were designed (Fig. 1), namely one for amplifying the sequences specific to DDSP (5′-GGA-TATTGTGTGCCAACTGC-3′ for the forward and 5′-GAGA-CAGGGTTTACACCATG-3′ for the reverse) and the other for amplifying the sequences specific to LCPTP/HePTP (5′-CAGCTGCTTCAGCAGACCTC-3′ for the forward and 5′-

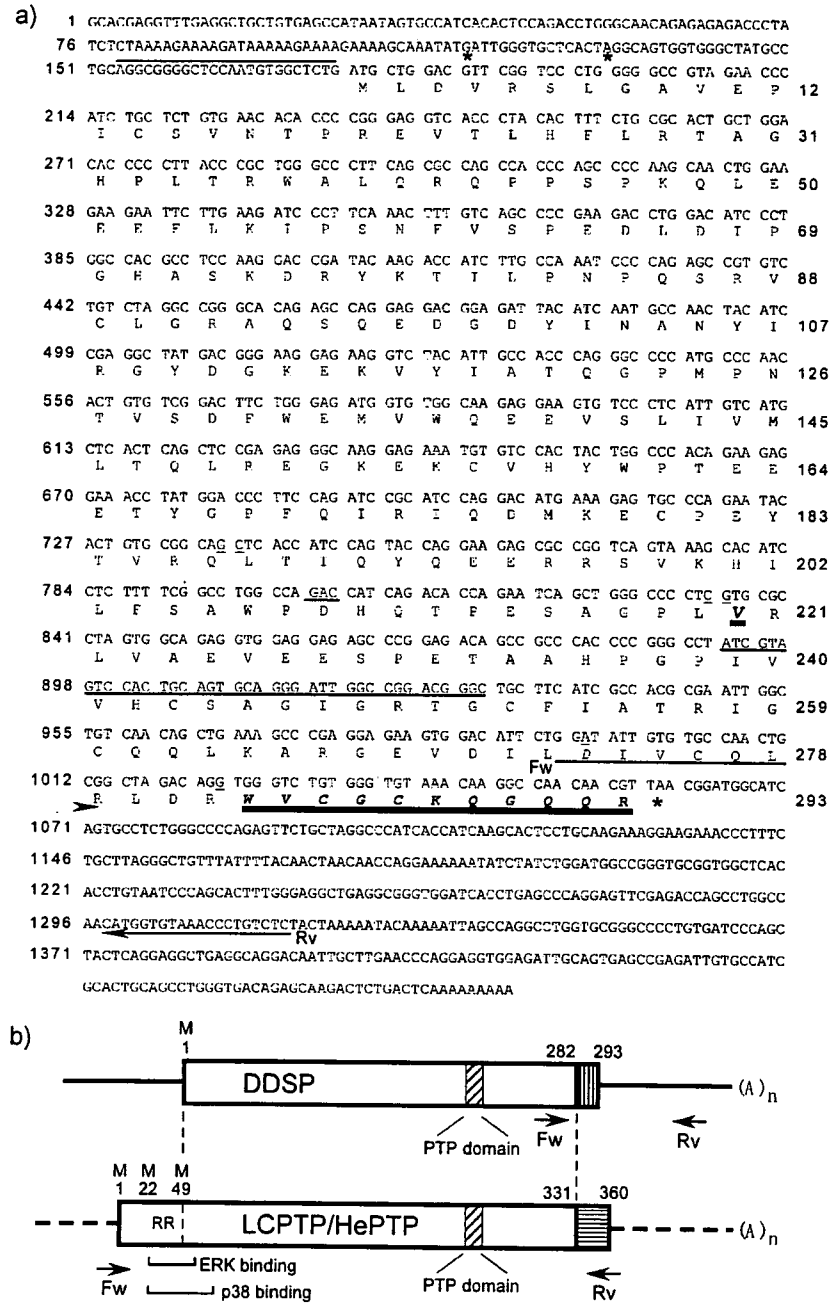

Fig. 1. The structure of DDSP. (a) The nucleotide and aa sequence of DDSP. The nucleotide number and the aa residue number are shown on the left side and right side, respectively. The substitution of the LCPTP/HePTP amino acid residues with the DDSP specific residues are highlighted by italic letters and bold lines, and the 2 termination codons are shown by asterisks. The putative PTP/DSP catalytic domain and Asp209, which is thought to be critical for PTP/DSP activity, are underlined. Arrows labeled with Fw and Rv are forward (Fw) and reverse (Rv) primers, respectively. (b) Schematic comparison of the DDSP structure with the LCPTP/HePTP structure. In DDSP, the aa residues required for ERK binding (including Arg41 and Arg42 shown as "RR" in the figure) are lacking (see text). The C-terminal 11 aa residues of DDSP (vertical bars) are different from those of LCPTP/HePTP (horizontal bars). The dashed box represents the PTP/DSP central catalytic domain. Arrows labeled with Fw and Rv are forward (Fw) and reverse (Rv) primers, respectively.

GGGGCTGGGTTCCTCAGGCA-3′ for the reverse). Tissue cDNA panels (Clontech Laboratories Inc.) were used for the RT-PCR.

2.5. Subcellular localization of DDSP

The full length DDSP cDNA sequence was ligated in-frame into pEGFP (Clontech), thus generating pDDSP-GFP in which the C′ -terminus of the DDSP sequence was fused to the N′ -terminus of green fluorescence protein (GFP). pDDSP-GFP was transfected into COS-7 cells and the cells were observed using a Leica TCS-SP System confocal laser microscope (Leica Microsystems). The cells were imaged for green fluorescence by excitation with the 488 nm line from an argon laser and the emission was viewed through a 496 to 505 nm band pass filter.

2.6. Immunocoprecipitation and Western blot analysis

For the immunocoprecipitation experiments, NIH3T3 mouse fibroblasts were transfected with a plasmid expressing flag-tagged DDSP using Superfect (Qiagen). At 24 h posttransfection, the cells were stimulated with 0.5 M NaCl for 20 min (for p38- and JNK-MAPK) or 50 ng/ml of PMA for 15 min after incubation in a serum free medium for 15 h (for ERK). Whole cell lysates were prepared by lysing the cells in a buffer (1.0% Nonidet P-40, 50 mM Tris–HCl pH 7.8, 150 mM NaCl, 1 mM DTT, 1 tablet of a protease inhibitor cocktail (Roche)). The lysates were incubated at 4 °C for 1 h with antibodies against ERK, JNK- or p38-MAPK (Cell Signaling) in an immunoprecipitation buffer (0.5% Nonidet P-40, 1 mM EDTA, 50 mM Tris–HCl pH 7.8, 200 mM NaCl, 1 mM DTT, 1 tablet of the protease inhibitor cocktail), and then further incubated with protein-A sepharose beads (Pharmacia) at 4 °C for 2 h. For Western blotting, the samples were separated by SDS-PAGE, transferred to a nitrocellulose filter, and then probed with an antibody against flag according to the manufacturer's protocol. To test the inactivation of the MAPK pathway by DDSP, two sets of transfection experiments were performed. In one experiment, the flag-tagged DDSP cDNA was transfected into NIH3T3 cells, and the transfected cells were then treated to activate ERK, p38 or JNK-MAPKs as in the immunocoprecipitation experiments. The transfection efficiency was monitored by the transfection of pEGFP in a separate dish and resulted in 30 to 50% efficiency. Western blotting was performed to observe the dephosphorylation of endogenous MAPK in the whole cell lysates of transfected cells using anti-phospho-MAPK antibodies (Cell Signaling). To observe the dephosphorylation of the endogenous activated MAPKs, the MACSelect system (Miltenyi Biotech) was used to enrich the transfected cells. The flag-tagged DDSP cDNA was ligated into the pMACSK^{k}II vector plasmid to generate pMACS-DDSP and the NIH3T3 cells were transfected in a 10 cm dish with 20 μg of pMACS-DDSP, or pMACSK^{k}II as a control. The transfected cells were subjected to affinity-column separation and then treated with 0.4 M sorbitol for 20 min to activate p38-MAPK, or 50 ng/ml of PMA for 15 min after incubation in a serum free medium for 20 h for ERK. Nearly 80% of the recovered cells were revealed to be transfected when the efficiency was preliminarily monitored by the cotransfection of pMACSK^{k}II and pEGFP. Western blotting was performed using anti-phospho-p38 or -ERK antibodies (Cell Signaling).

3. Results

3.1. Isolation of a cDNA sequence homologous to LCPTP/HePTP

Human T-cell leukemia cells (PEER) were treated with PMA and calcium ionophore A23187 to mimic TcR activation with (PEER(+)) or without (PEER(−)) 50 nM of DHEA. We performed the SSH screening by constructing a cDNA library in which the cDNAs from PEER(−) cells were subtracted from those from PEER(+) cells. After the SSH subtraction, the cDNAs for the MAPK phosphatases were enriched. One of these clones (named 1–20) contained 600 bases of sequence highly homologous to a leukocyte-specific PTP (LCPTP), also known as hematopoietic tissue-specific PTP (HePTP), a sequence which was originally isolated as a cytoplasmic PTP [19,20].

However, 1–20 contained another 150 bases of unique sequence and thus a phage cDNA library from the activated PEER cells was screened to obtain the full-length cDNA. The translation of the full length 1–20 (DDSP) cDNA sequence revealed one long open reading frame consisting of 293 amino acid (aa) residues, and also a striking homology (96% homology at the aa level) to LCPTP/HePTP (Fig. 1a). In the 50 aa residues of the LCPTP/HePTP N-terminus, there were 3 methionine (Met) residues: translation initiation Met 1 for LCPTP, translation initiation Met 22 for HePTP and Met 49 (Fig. 1b). A putative translation initiation Met for 1–20 corresponded to Met 49 of the LCPTP. And the preceding 24 nt of the 5′ noncoding sequence were identical to those of LCPTP/HePTP (sequence encoding aa residues 41 to 48 of LCPTP, as shown by the thin line above the nucleotide sequence preceding the translation initiation Met for 1–20 in Fig. 1a). However, about 150 bases of the sequence further upstream, including 2 in-frame termination codons, were unique. Although the aa sequence known as the PTP/DSP central catalytic domain was highly conserved, the striking homology to LCPTP/HePTP was disrupted at the C-terminal end, resulting in 11 novel aa sequences (Fig. 1a). Interestingly, the first 25 nt sequences encoding these 11 aa residues were identical to the partial sequence reported for the exon 9/intron 9 junction of LCPTP/HePTP [22].

A BLAST search of the human genome sequence using the 5′ - and 3′ -noncoding regions of 1–20 assigned each sequence to within the PTPN7 locus on chromosome 1q31 (the 5′ -noncoding sequence was the intron 2/exon 3 junction, and the 3′ -noncoding sequence was the read-through of the exon 9/intron 9 junction downstream to intron 9) that encodes LCPTP/HePTP, thus strongly suggesting that the 1–20 sequence was a novel alternatively spliced variant of the PTPN7 gene. Another RT-PCR experiment using RNA from human peripheral blood lymphocytes with or without reverse transcription confirmed that the full-length cDNA derived from the mRNA (data not shown).

3.2. Phosphatase activity

To test whether or not clone 1–20 possessed phosphatase activities, a GST fusion product with 1–20 was expressed in SF-9 insect cells since bacterially expressed fusion proteins always formed inclusion bodies. SDS-PAGE showed a stably expressed fusion protein with the expected molecular weight (data not shown). The expressed protein showed a rapid loss of phosphate from the phosphotyrosine in a time dependent manner. The activity was strongest at pH 6.0, and was suppressed by the PTP specific inhibitor sodium orthovanadate (Na_3VO_4) (Fig. 2a). In contrast to LCPTP/HePTP, the expressed 1–20 protein also caused a rapid loss of the phosphate from the phosphothreonine. Although threonine phosphatase activity was weaker (about 50% at the optimal pH 8.0) compared to tyrosine phosphatase activity at the optimal pH, the activity was suppressed by sodium fluoride (NaF), a serine/threonine phosphatase specific inhibitor (Fig. 2b).

3.3. Subcellular localization

The DDSP sequence was in-frame ligated into pEGFP generating pEGFP-DDSP which was transfected into COS-7 cells to observe the subcellular localization of GFP fluorescence. The GFP fluorescence was detected solely in the cytoplasm as in the case of LCPTP/HePTP. Furthermore, the distribution of the GFP-fluorescence was homogeneous, suggesting that this protein was not associated with the membrane structure (Fig. 3a). The treatment of the trans-

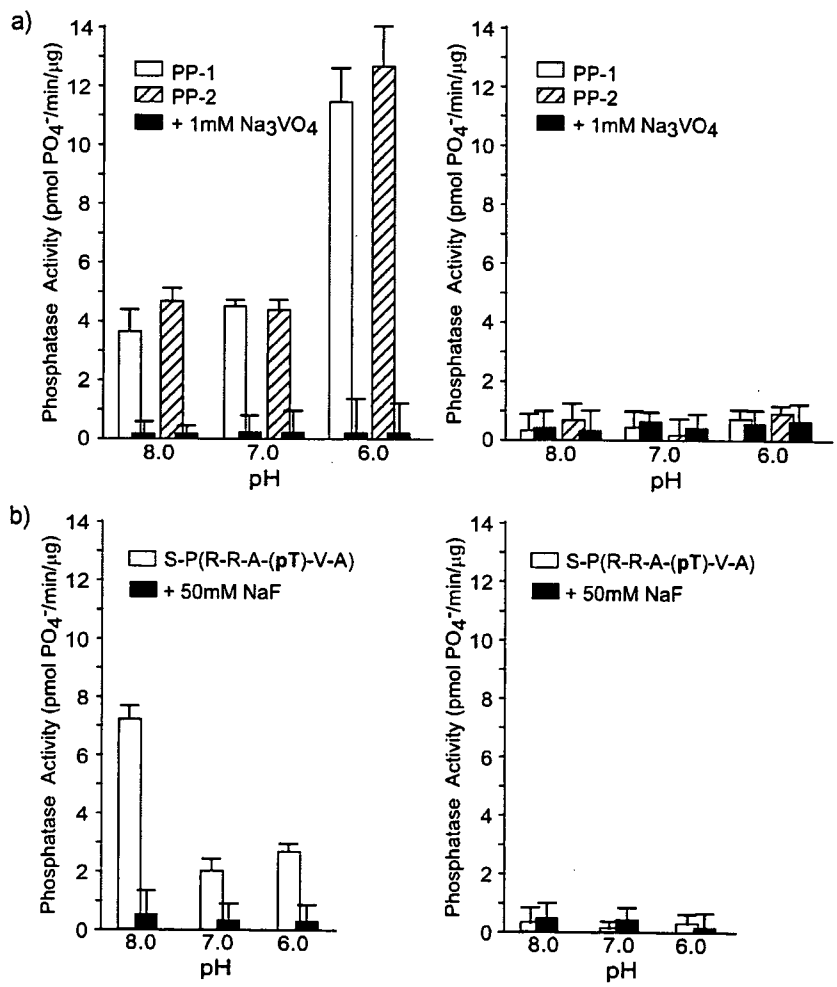

Fig. 2. Phosphatase activities of GST-DDSP. The sequence encoding GST-fused DDSP was ligated into the baculovirus expression vector and expressed in SF-9 cells. (a) Phosphotyrosine phosphatase activity of DDSP (left panel). PP-1 (open column) and PP-2 (dashed column) are 2 different kinds of phosphotyrosine substrate supplied by the manufacturer. Sodium vanadate (Na_3VO_4) is a PTP-specific inhibitor. The phosphatase activity was measured in the absence (open or dashed column) or presence (filled column) of 1 mM Na_3VO_4 and is shown as pmol phosphate released/min/μg of enriched cytosol after passage through a GST-affinity column. The right panel represents the activity of the sample from cells transfected with an empty vector plasmid. (b) Phosphothreonine phosphatase activity of DDSP (left panel). S-P is a phosphothreonine substrate. Sodium fluoride (NaF) is a serine/threonine phosphatase-specific inhibitor. The phosphatase activity was measured in the absence (open) or presence (filled column) of 50 mM NaF. The right panel represents the activity of the sample from cells transfected with an empty vector plasmid.